Bubble Formation and Dynamics in a Quiescent High-Density Liquid

Indrajit Chakraborty and Gautam Biswas
Dept. of Mechanical Engineering, Indian Institute of Technology, Kanpur 208016, India

Dept. of Mechanical Engineering, Indian Institute of Technology, Guwahati 781039, India

Satyamurthy Polepalle
ADS Target Development Section, Bhabha Atomic Research Centre, Mumbai 400085, India

Partha S. Ghoshdastidar
Dept. of Mechanical Engineering, Indian Institute of Technology, Kanpur 208016, India

DOI 10.1002/aic.14896

Gas bubble formation from a submerged orifice under constant-flow conditions in a quiescent high-density liquid metal, lead–bismuth eutectic (LBE), at high Reynolds numbers was investigated numerically. The numerical simulation was carried out using a coupled level-set and volume-of-fluid method governed by axisymmetric Navier–Stokes equations. The ratio of liquid density to gas density for the system of interest was about 15,261. The bubble formation regimes varied from quasi-static to inertia-dominated and the different bubbling regimes such as period-1 and period-2 with pairing and coalescence were described. The volume of the detached bubble was evaluated for various Weber numbers, We, at a given Bond number, Bo, with Reynolds number $Re \gg 1$. It was found that at high values of the Weber number, the computed detached bubble volumes approached a 3/5 power law. The different bubbling regimes were identified quantitatively from the time evolution of the growing bubble volume at the orifice. It was shown that the growing volume of two consecutive bubbles in the period-2 bubbling regime was not the same whereas it was the same for the period-1 bubbling regime. The influence of grid resolution on the transition from period-1 to period-2 with pairing and coalescence bubbling regimes was investigated. It was observed that the transition is extremely sensitive to the grid size. The transition of period-1 and period-2 with pairing and coalescence is shown on a Weber–Bond numbers map. The critical value of Weber number signalling the transition from period-1 to period-2 with pairing and coalescence decreases with Bond number as $We \sim Bo^{-1}$, which is shown to be consistent with the scaling arguments. Furthermore, comparisons of the dynamics of bubble formation and bubble coalescence in LBE and water systems are discussed. It was found that in a high Reynolds number bubble formation regime, a difference exists in the transition from period-1 to period-2 with pairing and coalescence between the bubbles formed in water and the bubbles formed in LBE. © 2015 American Institute of Chemical Engineers *AIChE J*, 61: 3996–4012, 2015

Keywords: numerical simulation, bubble formation, liquid metal, bubbling regimes, bubble volume, transition

Introduction

The growth and detachment of bubbles by injection of a gas through a submerged orifice in a quiescent liquid are of great interest for diverse applications in chemical, metallurgical, and biomedical systems.[1–4] Applications of gas bubble generation in high-density liquid metals include the operation of liquid metal circulation in metallurgical[5] and nuclear power systems.[6,7] In nuclear power systems,[6,7] the liquid metal lead–bismuth eutectic (LBE) is preferred as the target system taking into account the high production rate of neutrons, effective self-circulating heat removal, and minimal radiation damage. Few studies have been reported on the problem of bubble dynamics in liquid metals. Some experimental studies have focused on bubble formation and bubble rising in liquid metals.[8–14] Schwerdtfeger,[8] Mori et al.,[9] Eckert et al.,[10] Zhang et al.,[11] Andreini et al.,[12] Irons and Guthrie,[13] and Bai and Thomas[14] used different measuring techniques to evaluate the rise velocity and the drag coefficient, the shapes of the bubble, bubble size and bubble formation frequency in liquid metals. So far, not much research has been carried out concerning the effect of gas injection through submerged orifices or small holes in a liquid metal, because a liquid metal is not a transparent liquid and there are very few measuring techniques in experimental physics to evaluate the bubble diameters, bubble velocity, and bubble shape compared with transparent liquids, especially water. Considering these difficulties, numerical studies on the dynamics of bubble formation from an orifice in

---

Correspondence concerning this article should be addressed to G. Biswas at gtm@iitg.ernet.in or gautam721b@gmail.com.

a quiescent high-density liquid metal were undertaken in this work.

Many investigations of the basic case of bubble formation at a single orifice were reviewed by Kumar and Kuloor,[1] Clift et al.,[2] Kulkarni and Joshi,[4] Tsuge,[15] and Sadhal et al.[16] Different experimental studies[17–29] and theoretical approaches[30–38] were applied to study the problem of bubble formation at a single orifice or a single nozzle. In most of the theoretical models[17,18,22,32,33,38] developed by these workers, the effect of the previously formed bubble on the growth of the bubble at the orifice were not taken into account, although Zhang and Shoji,[21] Chuang and Goldschmidt,[39] and Deshpande et al.[40] developed models by taking into account the wake effect of the previous bubble or bubble coalescence. Depending on the operating parameters (gas flow rate, orifice diameter, surface wetting characteristics, and physical properties of the liquid phase), different regimes[19–21,23,26,27,41] are discerned as period-1, period-2 with pairing or double coalescence (see below), period-3 (triple coalescence), period-4 (quadruple coalescence), and finally chaotic bubbling regimes.[42] Most importantly, Higuera and Medina[35] reported that the period-2 regime consists of the pairing regime[20,21,23] and the double coalescence regime.[20,21,23] The pairing regime is characterized when two already detached bubbles rise as a pair and coalesce far away or near the orifice (detachment–detachment coalescence[34,35]). The double coalescence regime is defined when one already detached bubble coalesces with the growing bubble at the orifice (detachment–coalescence–detachment[34,35]). In this article, the behavior of the pairing regime is henceforward referred to as period-2 with pairing and coalescence bubbling regime.

Conversely, the dynamics of the growth and detachment of drops formed from a capillary tube in air have been extensively studied experimentally and numerically by Zhang and Basaran,[43] Wilkies et al.,[44] Yildirim et al.,[45] Ambravaneswaran et al.,[46–48] Subramani et al.,[49] and others. The period-1 dripping regime with or without satellite drop formation,[43–46] period-1 to complex dripping[47–49] (period doubling bifurcations, chaos, and hysteresis) to jetting,[48–50] and the transitions among different regimes have been discussed in detail.[47–51]

In addition to the experimental and theoretical investigations, numerical simulations of bubble formation processes have been carried out using the boundary integral method (BIM),[32–35,52] volume-of-fluid method,[53] level-set method,[54] coupled level-set and volume-of-fluid (CLSVOF) method,[55–60] and front tracking method.[61] Oguz and Prosperetti,[32] Higuera and Medina,[35] and Gordillo et al.[52] studied the bubble formation process from an orifice in a quiescent inviscous liquid at high Reynolds numbers by means of the potential flow approximation. Oguz and Prosperetti[32] did not discuss interactions between bubbles at high gas flow rates. Higuera and Medina[35] found a critical Weber number (high gas flow rates) for a given Bond number above which pairs of bubbles coalesce either in the vicinity of or far away from the orifice. However, the map of the transition between period-1 and period-2 bubbling regimes with a wide range of Bond and Weber numbers was not clearly shown. Gordillo et al.[52] reported numerical results of the characteristics of the minimum neck radius of the bubbles with time at high Reynolds numbers. Gerlach et al.,[55] Buwa et al.,[56] and Chakraborty et al.[57] used the CLSVOF method to evaluate the bubble formation process at a single submerged orifice under low and high gas flow rates. In their work, the effects of the orifice diameter,[56] gravity,[57] and gas flow rates on the period-1 and period-2 bubbling regimes and their transition characteristics[55,56] were reported. To the best of the authors' knowledge, there has been no numerical study to investigate the dynamics of bubble formation and rising in a high-density liquid metal as one of the fluids. The numerical investigation of bubble generation in a quiescent liquid with a high density ratio of liquid to gas, such as above 10,000, is a challenging task. For the design of efficient two-phase flow systems,[5–7] a detailed knowledge of the bubble sizes and shapes and different bubbling regimes is of fundamental importance.

The objective of this article is an *ab initio* numerical analysis of the effects of Weber and Bond numbers on the global characteristics of the bubble formation process at high Reynolds numbers, such as the frequency of the formation and the volume of bubbles created via injection of a gas at constant flow rate through a single orifice in quiescent high-density liquids. The combined level-set and volume-of-fluid (CLSVOF) method[57,58,62–64] was used to perform the numerical simulations. First, we validate our computational results with the benchmark scaling laws from very low to high flow-rate regimes of bubble formation. Then, we extend previous studies[32,35,56–58] to include time periodic bubbling regimes by means of qualitative and quantitative analyses, the interaction and coalescence behavior of bubbles in period-2 with pairing and coalescence bubbling regime, the transition between period-1 and period-2 with pairing and coalescence bubbling regimes characterized by a map that depends on *We* and *Bo* and a suitable scaling analysis for the transition. The analysis of other regimes (period-2 with double coalescence regime, period-3, period-4, and chaotic bubbling regimes) of bubble formation at sufficiently high gas flow rates was not investigated. It was observed that in period-2 with double coalescence regime, the coalesced bubble after departing from the orifice breaks up into toroidal bubbles due to strong liquid jet generation at the rear part of the coalesced bubble.[35] The axisymmetric solutions of the formation of toroidal bubbles are not realistic.[35] The three-dimensional (3-D) effect of the liquid wake or turbulent eddies stabilizes the shape and weakens the liquid jet[65] and no toroidal bubbles are formed. 3-D fluid flow was not taken into account in the present simulations. Therefore, numerical simulations using axisymmetric governing equations to study the problems of period-2 regime with double coalescence to the chaotic regime were not carried out.

In the present work, nitrogen and liquid LBE at atmospheric pressure and 220°C served as reference working fluids. Their physical properties are listed in Table 1. The effect of the nitrogen gas flow rate Q through the orifice in the range $0.5\,\text{mL/min} \leq Q \leq 140\,\text{mL/min}$ and the effect of the orifice radius R_o in the range $0.72\,\text{mm} \leq R_o \leq 3\,\text{mm}$ were studied. In this study, the five dimensionless parameters Weber number ($We = \rho_l Q^2/\pi^2 \sigma R_o^3$), Bond number ($Bo = \rho_l g R_o^2/\sigma$), Reynolds number ($Re = \rho_l Q/\pi R_o \mu_l$), density ratio of gas to liquid ($\eta = \rho_g/\rho_l$), and viscosity ratio of gas to liquid ($\lambda = \mu_g/\mu_l$) were provided for computations, where σ is the surface tension, ρ_l is the liquid density, ρ_g is the gas density, μ_l is the liquid viscosity, and μ_g is the gas viscosity. Quantitative and qualitative results were obtained by varying one dimensionless parameter while keeping other parameters fixed. We carried out investigations for $4.31\times10^{-4} \leq We \leq 24.81$, $0.13 \leq Bo \leq 2.28$, and $Re \gg 1$. The other two parameters were $\eta = 6.55\times10^{-5}$ [the ratio of the liquid (LBE) density to the gas density is about 15,261] and $\lambda = 1.12\times10^{-2}$. The orifice plate material was assumed to be a hydrophilic surface. In this

Table 1. Physical Properties of the Fluids for a Nitrogen–Liquid LBE System at $220^0 C$

Property	Value
ρ_l	10,443.4652 kg/m^3
ρ_g	0.684344 kg/m^3
μ_l	2.281×10^{-3} Pa s
μ_g	2.552×10^{-5} Pa s
σ	404.462×10^{-3} N/m

problem, the static contact angle was taken as $\phi_s = 0^0$, indicating that the bubble base is pinned to the orifice rim.

Formulation of the Problem

Problem description

The growth and detachment of gas bubbles at a single submerged orifice immersed in a quiescent liquid are discussed. When the gas flows through the orifice, the bubble volume increases continuously. According to classical Refs. 32 and 36, there are two stages of bubble formation, namely the expansion stage and the collapse stage. In the expansion stage, the bubble mainly grows in the radial direction and the detaching (upward direction) forces are weak compared with the attaching forces (downward direction). In the collapse stage, the bubble mainly grows in the axial direction (upward direction) and the detaching forces dominate over the attaching forces. In this stage, the bubble is attached to the orifice mouth through a neck forming in the vicinity of the orifice. At the end of this stage, the bubble is detached from the orifice and moves upwards through the liquid. In the present work, complete numerical simulation of the processes of bubble formation under constant-flow conditions[57,58] was performed using a cylindrical coordinate system $(r,\ z,\ \theta)$ as shown in Figure 1. The origin of the $(r,\ z,\ \theta)$ coordinate system is placed at the center of the orifice rim, where r is the radial coordinate, z is the axial coordinate measured in the opposite direction of gravity g, and θ is the azimuthal coordinate. In this article, the dynamics are assumed to be axisymmetric and the problem is independent of the azimuthal coordinate θ. A gas is injected at a constant flow rate Q through a single orifice of radius R_o at the horizontal hydrophilic bottom wall (wetting surface) submerged in a quiescent Newtonian liquid. We assume the ambient liquid and the gas filling the bubble to be incompressible with isothermal conditions. In the following, we discuss the different forces that act during the growth of the bubble at the orifice in a quiescent liquid.

At very low gas flow rates, the buoyancy (upward direction) and surface tension (downward direction) forces balance each other at the moment of bubble detachment[36] and the detached bubble volume V_F is determined by

$$2\pi R_o \sigma = V_F(\rho_l - \rho_g)g \tag{1}$$

where V_F is the Fritz volume[32,66] of a detached bubble which is assumed to be a sphere. This balance gives $V_F = 2\pi R_o\sigma/\rho_l g$ or $V_F^* = V_F/R_o^3 = 2\pi/Bo$ in dimensionless variables. The influence of ρ_g is neglected, since $\rho_g \ll \rho_l$ here. This regime of bubble formation is known as the quasi-static bubble formation regime[32,36,37] in which the bubble volume is independent of gas flow rate.

An inertia-dominated region of periodic bubbling exists at high gas flow rates.[17,18,32,35] In this high flow rate region, the bubble is detached when the buoyancy force has to overcome the force due to liquid inertia and the bubble volume can be estimated by an order of magnitude balance

$$\rho_l V_b g \sim \rho_l (Q/V_b^{2/3})^2 V_b^{2/3} \tag{2}$$

which yields $V_b \sim Q^{6/5}/g^{3/5}$ or, in dimensionless terms, $V_b/R_o^3 \sim (We/Bo)^{3/5}$.

The transition from the quasi-static region to the liquid inertia region can be characterized when the surface tension, buoyancy, and liquid inertia forces are all of the same order

$$\sigma R_o \sim \rho_l V_b g \sim \rho_l (Q/V_b^{2/3})^2 V_b^{2/3} \tag{3}$$

from which the critical gas flow rate[32] is defined by $Q_{cr} = \pi(16/3g^2)^{1/6}(\sigma R_o/\rho_l)^{5/6}$, which can be written in dimensionless form as $We_{cr} = (16/3)^{1/3} Bo^{-2/3}$. It can be found from Eqs. 1–3 that $V_b/V_F \sim (We/We_{cr})^{3/5}$, which is independent of Bond number. According to Ref. 32, V_b/V_F is constant when $Q \ll Q_{cr}$ $(We \ll We_{cr})$ and increases with $(Q/Q_{cr})^{6/5}$ $[(We/We_{cr})^{3/5}]$ when $Q \gg Q_{cr}$ $(We \gg We_{cr})$.

At the onset of the high-flow rate region, where the inertia of the liquid starts to influence the dynamics of the growing bubble at the orifice, the Reynolds number is of the order of $Re_{cr} = (\rho_l R_o \sigma/\mu_l^2)^{1/2}$ (obtained from Eq. 3). The Reynolds number is $Re_{cr} \sim 900$ for liquid LBE when the orifice radius $R_o = 1\ mm$, and higher Reynolds numbers are obtained for higher gas flow rates. This shows that in the present study, the effect of viscous force is very small during the process of bubble formation. However, the influence of liquid viscosity becomes important at the collapse stage of axisymmetric bubble collapse in a quiescent liquid, as reported by Thoroddsen et al.,[25] Gordillo,[67] and many others[68–71] in the case of pinch-off of liquid drops immersed in a fluid of negligible density when the minimum radius of the neck $R_{\min}$ becomes sufficiently small. Gordillo[67] found that viscous effects would not come into play in liquids with viscosities below 4.2 cP when $R_{\min} > 10\ \mu$m. In our present computations, it was found that the bubble pinched off when the minimum radius of the neck was $R_{\min} = 110\ \mu$m, as also suggested elsewhere.[58,61] Therefore, a very fine grid and very small time step are needed to capture the final instants prior to pinch-off. However, our computations are unable to resolve it owing to limitations of computational resources. Therefore, in LBE and water, the bubble pinch-off process also can be treated as an inviscid flow.

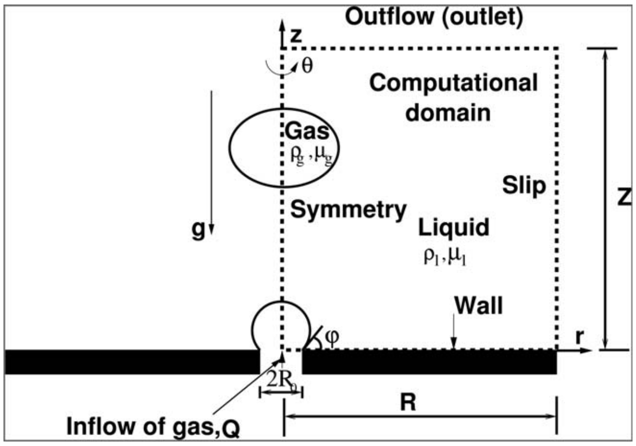

Figure 1. Schematic of bubble formation from an orifice and computational domain.

Governing equations and numerical method

In this study, the two-phase flow system consists of a gas and a liquid which are immiscible and incompressible fluids. It is assumed that the flow in each phase is axisymmetric. The problem is governed by the single set of continuity and Navier–Stokes equations for treating a single fluid continuum. The continuity equation is given in cylindrical axisymmetric coordinates (r, z) as

$$\frac{1}{r}\frac{\partial(ru)}{\partial r}+\frac{\partial v}{\partial z}=0 \tag{4}$$

where (u, v) are radial and axial components of the velocity field, respectively. The momentum equations are as follows:r direction

$$\rho(\tilde{\alpha})\left(\frac{\partial u}{\partial t}+u\frac{\partial u}{\partial r}+v\frac{\partial u}{\partial z}\right)=-\frac{\partial p}{\partial r}+\frac{\partial S_{rr}}{\partial r}+\frac{\partial S_{zr}}{\partial r} + \frac{S_{rr}}{r}+\rho(\tilde{\alpha})g_r+\sigma\kappa(\varphi)\frac{\partial\tilde{\alpha}}{\partial r} \tag{5}$$

z direction

$$\rho(\tilde{\alpha})\left(\frac{\partial v}{\partial t}+u\frac{\partial v}{\partial r}+v\frac{\partial v}{\partial z}\right)=-\frac{\partial p}{\partial z}+\frac{\partial S_{rz}}{\partial r}+\frac{\partial S_{zz}}{\partial z}+\frac{S_{rz}}{r} +\rho(\tilde{\alpha})g_z+\sigma\kappa(\varphi)\frac{\partial\tilde{\alpha}}{\partial z} \tag{6}$$

where p is the pressure, $g_r(=0)$, and $g_z(=-g)$ are the radial and axial components of the gravitational acceleration, respectively, and S_{rr}, S_{zz}, and S_{rz} are the components of Newtonian stress tensor, which are expressed as

$$S_{rr}=2\mu(\tilde{\alpha})\frac{\partial u}{\partial r},\ S_{zz}=2\mu(\tilde{\alpha})\frac{\partial v}{\partial z},\ and\ S_{rz}=S_{zr} =\mu(\tilde{\alpha})\left(\frac{\partial u}{\partial z}+\frac{\partial v}{\partial r}\right) \tag{7}$$

The influence of surface tension σ is incorporated into the momentum equations following the continuum surface force model of Brackbill et al.[72] Here, $\tilde{\alpha}$ is the smoothed void fraction field, which is defined using a Heaviside function,[62] $H_\varepsilon(\varphi)$, as

$$\tilde{\alpha}=H_\varepsilon(\varphi) =\begin{cases} 1 & \phi>\varepsilon \\ \dfrac{1}{2}+\dfrac{\phi}{2\varepsilon}+\dfrac{1}{2\pi}\left[\sin\left(\dfrac{\pi\phi}{\varepsilon}\right)\right] & |\phi|\le\varepsilon \\ 0 & \phi<-\varepsilon \end{cases} \tag{8}$$

where ϕ is the level set function, which is the signed distance function from the interface. ϕ is zero at the interface and has positive values in the liquid region and negative values in the gas region. Here, 2ε is the interface thickness over which the fluid properties are interpolated. The present simulations were performed using $\varepsilon=1.5\Delta r$, where Δr is the size of the computational cell. The smoothed density $\rho(\tilde{\alpha})$ and viscosity $\mu(\tilde{\alpha})$ can be expressed by a Heaviside function $H_\varepsilon(\phi)$ as

$$\rho(\tilde{\alpha})=\rho_l\tilde{\alpha}+\rho_g(1-\tilde{\alpha}) \tag{9}$$

$$\mu(\tilde{\alpha})=\mu_l\tilde{\alpha}+\mu_g(1-\tilde{\alpha}) \tag{10}$$

where subscripts l and g represent liquid and gas, respectively. The density and viscosity of the liquid and gas are assumed to be constant. The local curvature κ at the gas–liquid interface is computed as

$$\kappa=-\nabla.\hat{n} \tag{11}$$

where the unit normal vector $\hat{n}$ is derived from level set function ϕ

$$\hat{n}=\frac{\nabla\phi}{|\nabla\phi|} \tag{12}$$

and it is directed into the liquid region. In the CLSVOF method, the advection equations for the volume fraction α and the level set function ϕ are

$$\frac{\partial\alpha}{\partial t}+\frac{1}{r}\frac{\partial(r\alpha u)}{\partial r}+\frac{\partial\alpha v}{\partial z}=0 \tag{13}$$

$$\frac{\partial\phi}{\partial t}+u\frac{\partial\phi}{\partial r}+v\frac{\partial\phi}{\partial z}=0 \tag{14}$$

The governing equations are nondimensionalized by introducing nondimensional variables using $r^*=\frac{r}{R_o}$, $z^*=\frac{z}{R_\mathrm{o}}$, $\kappa^*=\kappa R_o$, $u^*=\frac{u}{v_\mathrm{d,avg}}$, $v^*=\frac{v}{v_\mathrm{d,avg}}$, $p^*=\frac{p}{\rho_l v_\mathrm{d,avg}^2}$, $t^*=\frac{tv_\mathrm{d,avg}}{R_\mathrm{o}}$, $\rho^*(\tilde{\alpha})=\frac{\rho(\tilde{\alpha})}{\rho_1}$, and $\mu^*(\tilde{\alpha})=\frac{\mu(\tilde{\alpha})}{\mu_1}$ where the orifice radius R_o is the characteristic length and average inflow velocity of gas at the orifice inlet $v_{d,avg}(=Q/\pi R_o^2)$ is the characteristic velocity. The resulting governing equations[58] are as follows:

Continuity equation:

$$\nabla.\vec{V}^*=0 \tag{15}$$

Momentum equations

$$\rho^*(\tilde{\alpha})\left(\frac{\partial\vec{V}^*}{\partial t^*}+\nabla.\left(\vec{V}^*\vec{V}^*\right)\right) =-\nabla p^*+\rho^*(\tilde{\alpha})\left(\frac{Bo}{We}\right)+\left(\frac{1}{Re}\right)\nabla.\left[\mu^*(\tilde{\alpha})\left(\nabla\vec{V}^*+\left(\nabla\vec{V}^*\right)^T\right)\right] +\left(\frac{1}{We}\right)\kappa^*(\varphi)\nabla\tilde{\alpha} \tag{16}$$

where $\vec{V}=(u, v)$ is the velocity vector. In Eq. 16, the density and viscosity of the single fluid continuum are computed by

$$\rho^*(\tilde{\alpha})=\tilde{\alpha}+\eta(1-\tilde{\alpha}) \tag{17}$$

$$\mu^*(\tilde{\alpha})=\tilde{\alpha}+\lambda(1-\tilde{\alpha}) \tag{18}$$

Additionally, we shall provide two other parameters, the Froude number $Fr=\frac{v_{d,avg}^2}{gR_o}\left(=\frac{We}{Bo}\right)$ and the Ohnesorge number $Oh=\frac{\mu_l}{\sqrt{\rho_l R_o\sigma}}\left(=\frac{\sqrt{We}}{Re}\right)$. In this study, the range of the Ohnesorge number is $0.0006 < Oh < 0.0013$ and the range of the Reynolds number is $10 < Re < 4000$.

The CLSVOF numerical method[57,62] for an evolving moving interface was implemented in the present study. In the CLSVOF method, the level set function[73] ϕ is used to capture the interface and volume of the fluid fraction[74] α is used to conserve mass due to the moving interface. The governing equations are discretized using the finite-difference method on an axisymmetric coordinate and equidistant grid $\Delta r=\Delta z$ in the radial and axial directions. The MAC algorithm[75] is employed to solve the single set of governing equations on a

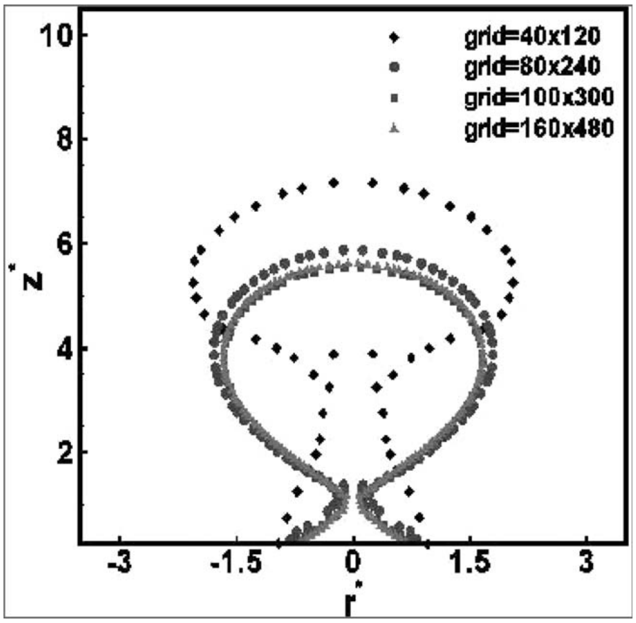

Figure 2. Effect of mesh size on bubble shape at departure for $Q = 1.67\times10^{-7} m^3/s$, $R_o = 1\times10^{-3}$m in a nitrogen–liquid metal LBE system.

The nondimensional numbers are $We = 0.0727$, $Bo = 0.253$, $Re = 242.33$, $\eta = 6.55\times10^{-5}$, and $\lambda = 0.0112$.

staggered grid with scalars (p,ϕ, and α) located at the cell centers and velocity components ($\vec{V}$) at the center of the cell faces. The convection and the viscous terms are discretized by a second-order ENO method[63] and central differencing, respectively. In the present work, the time stepping procedure is based on the explicit method to maintain the stability of the solution. During the computations, time steps are chosen to satisfy CFL, capillary, viscous and gravitational time conditions (discussed in Section 2.3 in Ref. 76). The details of the numerical method have been described by Chakraborty et al.[76]

Computational domain and boundary conditions

The computational domain established for axisymmetric numerical simulations of bubble formation is shown in Figure 1. For low and high gas flow rates involved in the present problem, the width and height of the computational domain are taken as $R = 20R_o$ and $Z = 60R_o$, respectively, so that the bubble formation process is unaffected by the side and outflow boundaries, as also discussed elsewhere.[58]

As boundary conditions, symmetry or slip condition at the left or right boundaries, no-slip condition at the bottom wall and Neumann condition at the outflow boundary are imposed. At the orifice inlet, gas flows upwards with a defined parabolic profile of Poiseuille flow.[57,58] At the orifice, the Reynolds number $Re_g\left(=\frac{\rho_g v_{d,avg} D_o}{\mu_g}\right)$ based on the gas properties is deployed, where D_o is the orifice diameter. The range of Re_g is below of the laminar pipe flow condition ($Re_g < 2300$). To ensure incompressibility in the flow domain, a "reference" pressure p_{ref} of the liquid is applied at a particular point for all the computations. In these simulations, $p_{ref} = 0$ is applied as the reference pressure. At the outflow boundary (outlet) the pressure is the "reference" pressure (p_{ref}) minus the hydrostatic pressure $p(r,Z,t) = p_{ref} - \rho_l(-g)Z = -\rho_l(-g)Z$. At the bottom wall, Neumann condition of the pressure is applied. The bubble is initially assumed to be a hemisphere of radius equal to the orifice radius. Both the gas phase and the liquid phase are assumed initially to be quiescent and at uniform pressure.

Grid independence test and validation

The grid independence test is performed using 40 × 120, 80 × 240, 100 × 300, and 160 × 480 mesh grids in a computational domain, as shown in Figure 2 for the conditions $We = 0.0727$, $Bo = 0.253$, and $Re = 242.33$. The period-1 bubbling regime (see below in the Results section) can be observed under these conditions. Figure 2 shows the difference between profiles at the final instant prior to bubble pinch-off. The maximum relative difference in height of the profiles obtained is around 21.92% for 40 × 120 and 80 × 240 mesh grids, around 6.22% for 80 × 240 and 100 × 300 mesh grids and around 1.33% for 100 × 300 and 160 × 480 mesh grids. Figure 2 also reveals that the bubble shapes before detachment of the bubble for 100 × 300 and 160 × 480 mesh grids are almost identical, but very different from those for 40 × 120 and 80 × 240 mesh grids.

In addition to the above analysis, the volume of a detached bubble is calculated using 40 × 120, 80 × 240, 100 × 300, and 160 × 480 mesh grids with the same parameters as in Figure 2. Table 2 shows the volumes of detached bubbles for different mesh grids. The difference in detached bubble volume for 40 × 120 and 80 × 240 mesh grids is around 6.43%, for 80 × 240 and 100 × 300 mesh grids it is around 24% and for 100 × 300 and 160 × 480 mesh grids it is around 0.3%. Therefore, in this study, the computations were performed on 100 × 300 mesh grids to save computing time without affecting the accuracy of the numerical results. Depending on the orifice radius R_o and volumetric gas flow rate Q through the orifice, a grid resolution $\Delta r = \Delta z = 0.2\times10^{-3}$ m in both the r and z directions was chosen to capture the bubble formation process accurately. The corresponding uniform dimensionless mesh size of $\Delta r/R_o = \Delta z/R_o = 0.2$ was employed in all simulations in both directions. During our computations, the time step was chosen as $\Delta t = 10^{-6}s$ to satisfy the Courant–Friedrichs–Lewy (CFL) and capillary time step conditions.[76]

The computed volume of a dimensional detached bubble for this case is $V_b = 2.2585\times10^{-8}$ m^3. The calculated detached bubble volumes from the analytical correlations given by Jamialahmadi et al.[22] and Gaddis and Vogelpohl[38] are $V_b = 2.407\times10^{-8}$ m^3 and $V_b = 2.520\times10^{-8}$ m^3, respectively. The comparison shows good agreement with the analytical correlations[22,38] resulting in errors of about 6.17% and 10.38 % relative to the analytical correlations of Jamialahmadi et al.[22] and Gaddis and Vogelpohl,[38] respectively. The discrepancy found in the bubble volume in LBE between the predicted result and the studies of Jamialahmadi et al.[22] and Gaddis and Vogelpohl[38] is due to the spherical bubble assumption in the latter models. The accuracy of the correlation given in Ref. 38 was assessed with the experimental results for highly viscous liquids. The volume of a detached

Table 2. Volume of Detachment Bubble vs. Mesh Grid in the Nitrogen–LBE System Under the Conditions $We = 0.0727$, $Bo = 0.253$, $Re = 242.33$, $\eta = 6.55\times10^{-5}$, and $\lambda = 0.0112$

Number of grid meshes	Detached bubble volume ($\times10^{-8} m^3$)
40×120	2.981
80×240	2.801
100×300	2.2585
160×480	2.265

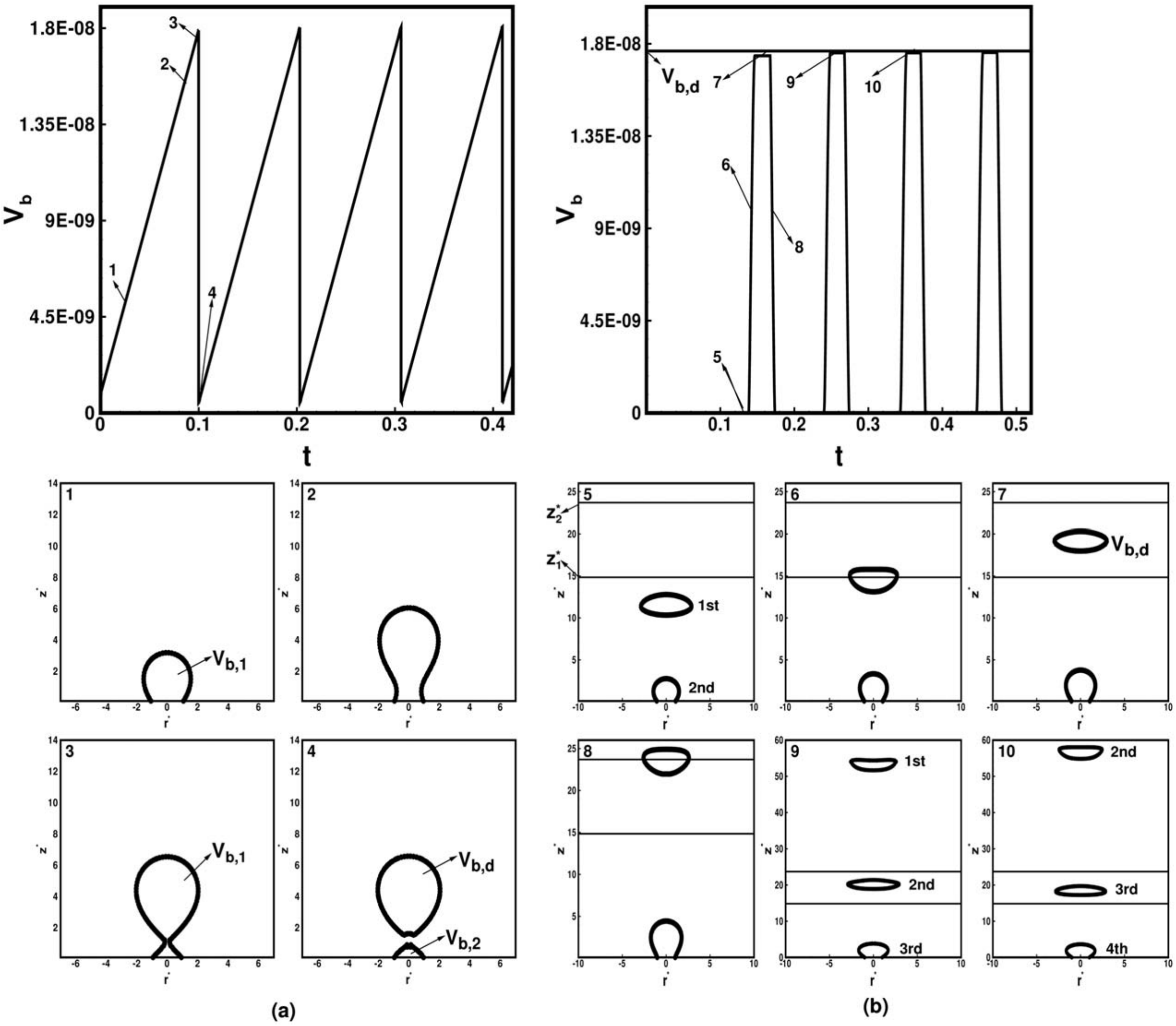

Figure 3. (a) Time evolution of the volume of four consecutive bubbles (top) and time instant of first bubble growth and breakup (bottom) at the orifice and (b) volume of detached bubbles (top) after bubble breakup and the generation of bubbles (bottom) under the conditions $We = 0.172$, $Bo = 0.1425$, $Re = 325.09$, $\eta = 6.55\times10^{-5}$, and $\lambda = 0.0112$.

bubble in water using the same geometric and flow conditions, leading to $Bo = 0.1363$, $We = 0.0391$, and $Re = 53.05$, is $V_b = 3.9\times10^{-8} m^3$, obtained by Gerlach et al.[55] (see Table 2 in Ref. 55). It is observed that the detached bubble volume in LBE is smaller than that in water for low gas inflow rate conditions when the static contact angle $\varphi_s = 0^0$. This is primarily due to higher Bond number leading to a higher buoyancy force compared with the surface tension force at the bottom of the growing bubble in LBE than that of water. This effect causes early detachment of the bubble in LBE. However, Irons and Guthrie,[13] Bai and Thomas,[14] and Gnyloskurenko and Nakamura[77] found that the average bubble sizes in liquid metal are larger than those of air bubbles in water. This may be due to the lower Bond numbers used in liquid metals compared with those in water. It was also reported[13,14,77] that the dynamics of the bubble formation process in a liquid metal were also influenced by the presence of nonwetting or hydrophobic materials with $\varphi_s > 90^0$ (referred to as poor wettability). This influences the bubble base diameter along the surface material and the final detached bubble volume. Gnyloskurenko et al.,[28] Byakova et al.,[29] Lin et al.,[78] and Corchero et al.[79] experimentally and Gerlach et al.[55] numerically found that the size of the detached bubble is controlled by the orifice diameter when $0^0 \leq \varphi_s < 68^0$ (referred to as good wettability) and is independent of the contact angle. It was found that when $\varphi_s < 68^0$ the bubble base coincides with the edge of the orifice during the bubble formation process. In the present work, the effect of the contact angle was not considered. Therefore, studies on the problem of the dynamics of bubble formation on hydrophobic surfaces are beyond the scope of the present work.

Unfortunately, the dynamics of bubble formation for different materials (with different static contact angles φ_s), both hydrophilic and hydrophobic, in liquid metal LBE systems are lacking in the literature. To justify the accuracy of our numerical code, computations were carried out to determine the volume of detached bubbles in argon–liquid aluminum, where the liquid density and surface tension are $\rho_l = 2373\,\mathrm{kg/m^3}$ and $\sigma = 860\times10^{-3}\,\mathrm{N/m}$, respectively, when $\varphi_s = 0^0$. The computed results are compared with the experimental results of Gnyloskurenko and Nakamura[77] and Gnyloskurenko et al.,[28] where the gas flow rates injected through the orifice of radius $R_o = 0.5\times10^{-3}\,\mathrm{m}$ are $Q = 0.648\times10^{-6}\,\mathrm{m^3/s}$ for liquid

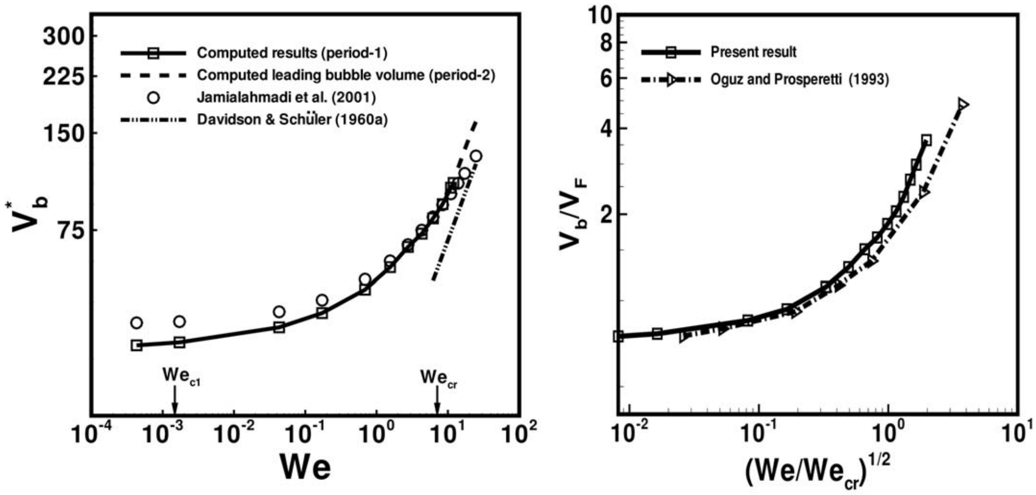

(a) (b)

Figure 4. (a) Dimensionless detached bubble volume $V_b^* = V_b/R_o^3$ as a function of Weber number *We* for $Bo = 0.1425$, $13.06 \le Re \le 3140.51$, $\eta = 6.55\times10^{-5}$, and $\lambda = 0.0112$. The computed bubble volume in the period-1 regime is represented by the solid line with square symbols. The dashed line gives the volume of the first (leading) bubble of each pair in the period-2 with pairing and coalescence regime. The results represented by circle symbols were obtained by the correlation of Jamialahmadi et al.[22] In the high Weber number regime, $We \ge 6.38$, the dashed-dotted dotted line denotes the bubble volume obtained by the correlation of Davidson and Schuler.[17] (b) The volume of a detached bubble V_b normalized by the Fritz volume V_F vs. $(We/We_{cr})^{1/2}$.

The results denoted by the dashed-dotted line with triangle symbols were obtained from the numerical simulation of Oguz and Prosperetti[32] (see Figure 2 in Ref. 32).

aluminum ($Bo = 0.0067$ and $We = 0.933$) and $Q = 0.033\times10^{-6}\,m^3/s$ for water ($Bo = 0.034$ and $We = 0.0122$) under low flow rate conditions. The detached volumes obtained from present computations and experiments are $1.81\times10^{-7}\,\mathrm{m}^3$ and $1.70\times10^{-7}\,\mathrm{m}^3$, respectively (see Ref. 78), with an error of 6.47% in liquid aluminum. The corresponding values in the air–water system are $2.81\times10^{-8}\,\mathrm{m}^3$ and $2.84\times10^{-7}\,\mathrm{m}^3$, respectively (see Ref. 28), with an error of 1.06%. The discrepancy between our results and the results in Refs. 28 and 77 may be due to the flow rate conditions with time at the orifice in the latter experiments. It is observed that the volume of bubbles is larger in liquid aluminum than in water, which can be attributed to the differences in buoyancy forces in water and liquid aluminum metal systems. Gnyloskurenko et al.[28] and Gnyloskurenko and Nakamura[77] found that the volume of a detached bubble is independent of φ_s in the range $0 \le \varphi_s < 68^0$. Therefore, the present results are valid for the wetting or hydrophilic materials with $0 \le \varphi_s < 68^0$.

Results

In this section, we examine bubble generation and bubble dynamics in a high-density liquid metal (liquid LBE). We discuss growing and detached bubble volumes, bubble formation frequency, and the features of the period-1 and period-2 with pairing and coalescence bubbling regimes.

Calculation of detached bubble volume

In this section, the calculation of the dimensional detached bubble volume (V_b) is discussed under the conditions of $Q = 1.67\times10^{-7}\,\mathrm{m}^3/s$ and $R_o = 0.75\times10^{-3}\,\mathrm{m}$, as shown in Figure 3. The bubble volume V_b is defined as

$$V_b = \int_V (1-\alpha)dV \tag{19}$$

where

$$dV = 2\pi r\Delta r\Delta z \tag{20}$$

α is the liquid volume fraction and V is the volume of the computational domain covering growing or detached bubbles. In Figure 3a, the top diagram shows the evolution of the dimensional growing bubble volume at the orifice for four consecutive bubbles with dimensional time and the bottom diagrams show the time sequence of the first growing bubble at the orifice and its detachment. In Figure 3b, the top diagram shows the corresponding detached bubble (rising bubble) volume calculated within a certain height of the computational domain (between z_1^* and z_2^*) after bubble breakup and the bottom diagrams show the corresponding detached bubbles moving through the ambient liquid. In Figure 3a, the detached bubble volume $V_{b,d}$ is calculated as

$$V_{b,d} = (V_{b,1} - V_{b,2}) \tag{21}$$

where $V_{b,1}$ is the bubble volume just before bubble detachment [where the arrow indicates 3 at the top of Figure 3a]. When the bubble is detached, it leaves another small bubble, with volume $V_{b,2}$ [where the arrow indicates 4 at the top of Figure 3a] attached to the orifice. In Figure 3b, arrows 5–8 indicate the volumes of first rising bubble through distances between z_1^* and z_2^* and arrows 9 and 10 denote the volumes of second and third detached bubbles. The results show that the first detached bubble has a smaller volume than those of the second, third, and fourth detached bubbles, which have the same volume. It can be concluded for this case that the bubble formation process reaches a stable state after first bubble detachment for low Weber numbers, that is, for low gas flow rates.[59]

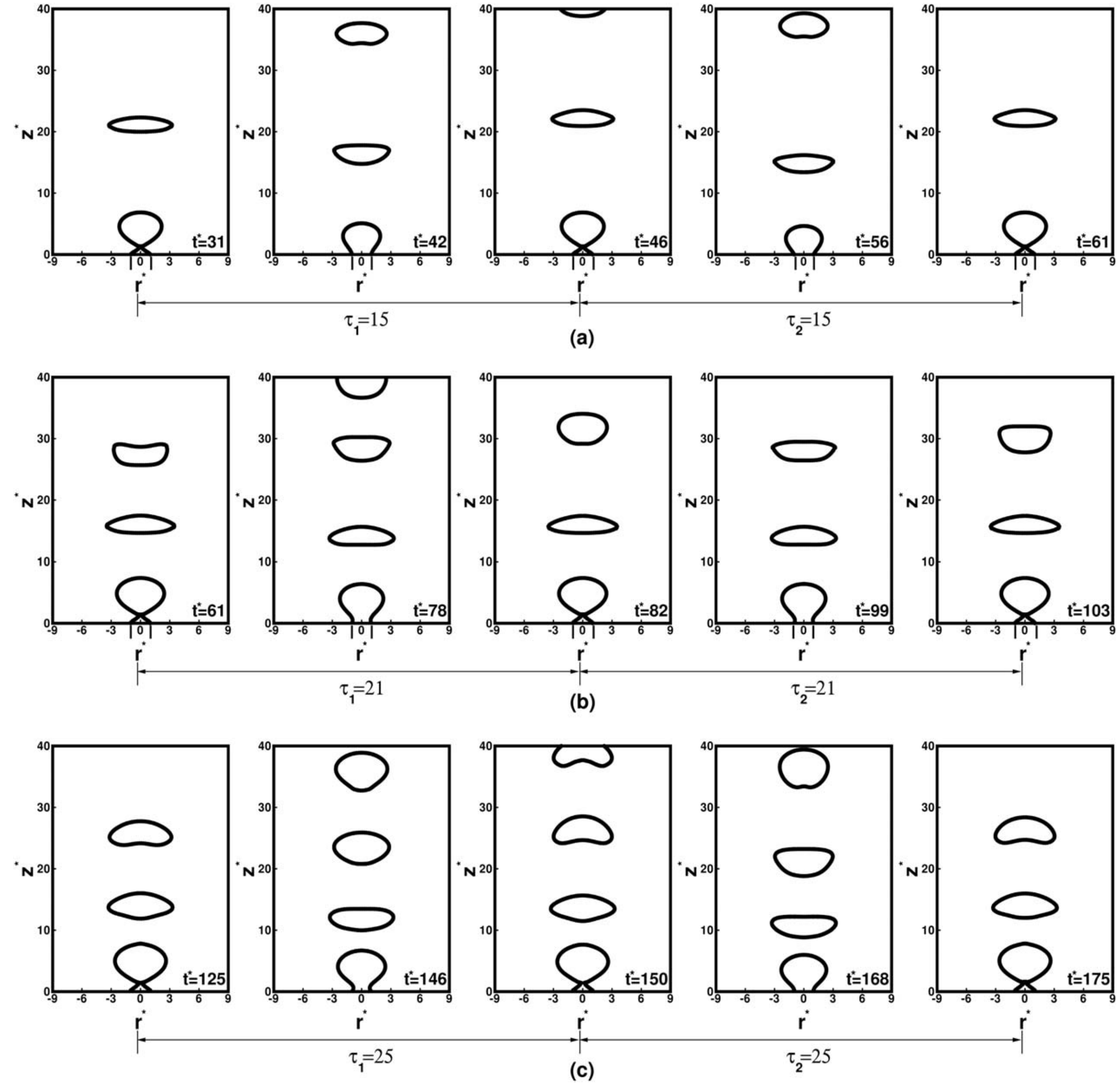

Figure 5. Period-1 bubbling regime for $Bo = 0.1425$ and various values of We and Re.

(a) $We = 0.69$, $Re = 530.77$; (b) $We = 2.76$, $Re = 1061.54$; and (c) $We = 6.20$, $Re = 1550$. The others two parameters are $\eta = 6.55\times 10^{-5}$ and $\lambda = 0.0112$.

Regimes of low, intermediate and high Weber numbers (gas flow rates)

The dimensionless detached bubble volume $V_b^*(=V_b/R_o^3)$ as a function of Weber number or gas flow rate is shown in Figure 4a when $Bo = 0.1425$ and the range of the Weber number is $4.31\times 10^{-4} \le We \le 24.81$. Figure 4a shows that the influence of Weber number (gas flow rate, Q) on the volume of detached bubble is significant, and three regimes of the dynamics of bubble formation are observed. For Weber numbers in the range $4.31\times 10^{-4} \le We \le We_{c1}$, the volume of a detached bubble is constant and independent of We, where the computed value of $We_{c1} = 1.7\times 10^{-3}$, which is the critical Weber number (gas flow rate) below which the force due to liquid inertia caused by the bubble growth at the orifice exit is neglected and the surface tension force dominates over buoyancy force. The dynamics in this range exhibit a low Weber number region. In this region, the bubble grows quasi-statically (discussed in the section Formulation of the Problem) until the buoyancy force overcomes the surface tension confinement force. In the quasi-static regime, the computationally predicted value of detached bubble volume is $V_b^* = 33.1$. For comparison, the Fritz volume is $V_F^* = 44.09$ (see the section Formulation of the Problem) when $Bo = 0.1425$. It is noteworthy that the ratio of computed detached bubble volume to Fritz volume is $V_b^*/V_F^* = 0.7507$. Our computed volume is smaller than the Fritz volume due to the deviation from an equilibrium spherical shape at its detachment.[24,32,58] The Bond number based on the size of the bubble at detachment is $(\rho_l g V_b^{2/3})/\sigma = Bo\times(V_b^*)^{2/3}$, which is greater than one, and the bubble at detachment is not spherical. When the Weber number exceeds the critical value $We = We_{c1}$, the inertia of the liquid comes into play during bubble growth at the orifice and

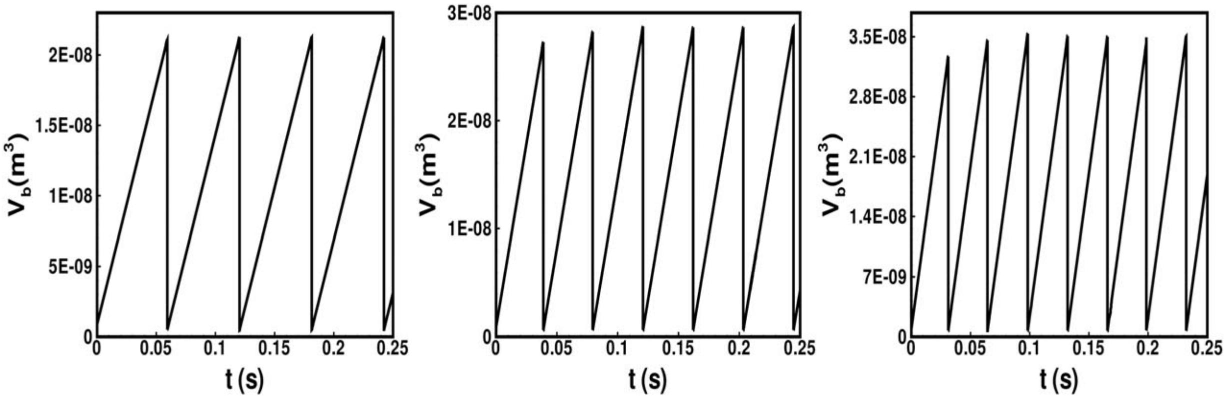

(a) We = 0.69 **(b)** We = 2.76 **(c)** We = 6.20

Figure 6. Time evolution of the growing bubble volume at the orifice in the period-1 bubbling regime for *Bo* = 0.1425 under the conditions (a) *We* = 0.69, (b) *We* = 2.76, and (c) *We* = 6.20.

the bubble volume increases with We. For the range $We_{c1} \leq We < We_{cr} = 6.38$ (see the section Formulation of the Problem for We_{cr}), an intermediate Weber numbers region is discerned, where the inertia of the liquid adds to the surface tension force and opposes the buoyancy force during the bubble detachment. At $We = We_{cr}$, the critical Weber number (gas flow rate) above which the opposing force of bubble growth due to liquid inertia can no longer be neglected and the influence of surface tension confinement force decreases. Beyond We_{cr}, with increasing We, the bubble volume V_b^* increases significantly with We. The results in Figure 4a show that the volumes converge toward the results obtained from the correlation $V_b = 1.378(Q^{6/5}/g^{3/5})$ or $V_b^* = \frac{V_b}{R_o^3} = 5.4395\left(\frac{We}{Bo}\right)^{3/5}$ given by Davidson and Schuler[17] for high Weber numbers. The results indicate that at high We the bubble volume follows the 6/5 power of the gas flow rate or the 3/5 power of the Weber number. The deviation between our results and the correlation of Davidson and Schuler[17] is due to the single-stage model assuming the bubble to be growing spherically in the high We region reported by Ref. 17. For $We \geq 13.95$, the bubbles start to rise in pairs and coalesce far away from the orifice (see below), known as period-2 with pairing and coalescence bubbling regime. The results in Figure 4a show that for $We \geq 13.95$ the computed bubble volume is the leading bubble volume of each pair represented by the dashed line. The numerical calculations of bubble volume reveal good quantitative agreement with the analytical correlation given by Jamialahmadi et al.[22] The present results show a qualitatively similar trend to the results obtained by Oguz and Prosperetti[32] (as shown in Figure 2 in Ref. 32) and Higuera and Medina[35] (as shown in Figure 2 in Ref. 35). The numerical results of Higuera and Medina[35] cover the range of Weber numbers $0.1 \leq We \leq 25328.72$ with $Bo = 0.1$ and 1.0, $\eta = 0.001$ and $\lambda = 0.01$. Those of Oguz and Prosperetti[32] cover wide ranges of Weber numbers, $0.0017 \leq We \leq 72513.601$, and Bond numbers, $0.0014 \leq Bo \leq 0.545$, $\eta = 0.001$ and $\lambda = 0.01$. Further, the comparisons between our computed results and the numerical results of Oguz and Prosperetti[32] based on the BIM are shown in Figure 4b, where the volume of detached bubbles scaled with the Fritz volume V_F is plotted as a function of $(We/We_{cr})^{1/2}$ (see the section Formulation of the Problem). It is observed that the present results match the results of Oguz and Prosperetti[32] reasonably well. As can be seen from Figure 4, the present numerical simulations were not carried out beyond $We > 24.81$ or $(We/We_{cr})^{1/2} \geq 2$, the reason being that the coalesced bubble formed in period-2 with pairing and coalescence breaks up, leading to toroidal bubble formation (not shown here) for the nitrogen–LBE system. The results in Figure 4 depict that the present simulations cover bubble formation from a quasi-static regime in the very low Weber number region to an inertia-dominated regime in the high Weber number region.

We report the results of numerical simulations performed for the investigations of period-1 and period-2 with pairing and coalescence bubbling regimes. Grid sensitivity analysis of both regimes was performed using $\Delta r/R_o = \Delta z/R_o \approx 0.333$, $\Delta r/R_o = \Delta z/R_o = 0.2$, and $\Delta r/R_o = \Delta z/R_o = 0.1$ grid sizes. The dynamics of bubble formation using $\Delta r/R_o = \Delta z/R_o = 0.2$ and $\Delta r/R_o = \Delta z/R_o = 0.1$ grid sizes showed almost no significant difference (not shown here) in the two regimes. Therefore, the simulations were carried out on a 100×300 mesh grid with a uniform dimensionless mesh size of 0.2 in both directions. Figure 5 shows the period-1 bubbling regime at $Bo = 0.1425$ for (a) $We = 0.69$, (b) $We = 2.76$, and (c) $We = 6.20$. The simulation corresponds to nitrogen bubble formation in a liquid metal LBE and the Morton number ($M = g\mu_l^4/\rho_l\sigma^3$) of the liquid is 3.84×10^{-13}. The diameter of the detached bubble becomes larger than the diameter of the orifice owing to continuous injection of a constant air flow rate at the orifice. Figure 5 depicts that for each value of We, the shape of the rising bubble deviates from spherical and oscillates after detachment. At such a low value of M and a moderate bubble size, the liquid inertia force dominates and shape oscillation can be observed.[2,80] Figure 5a indicates that at low We (low gas flow rate) the detached bubble rises sufficiently away from the orifice. With further increase in We (increasing gas flow rate), the distance between the bubbles decreases, as shown in Figures 5b, c. However, the influence of the wake behind the rising (leading) bubble on the growing bubble (trailing bubble) at the orifice becomes insensitive and therefore no interaction can be observed. Qualitatively, the results in Figure 5 show that a regular train of nearly identical bubbles of equal size is produced from the orifice. In addition to the equal size, the bubbles are seen to form above the orifice at equal intervals of dimensionless time $\tau_1 = \tau_2$, where the bubble detachment period τ is defined as the time interval between the detachment instant of a bubble and that of the next bubble. Figure 6 shows the time evolution of the

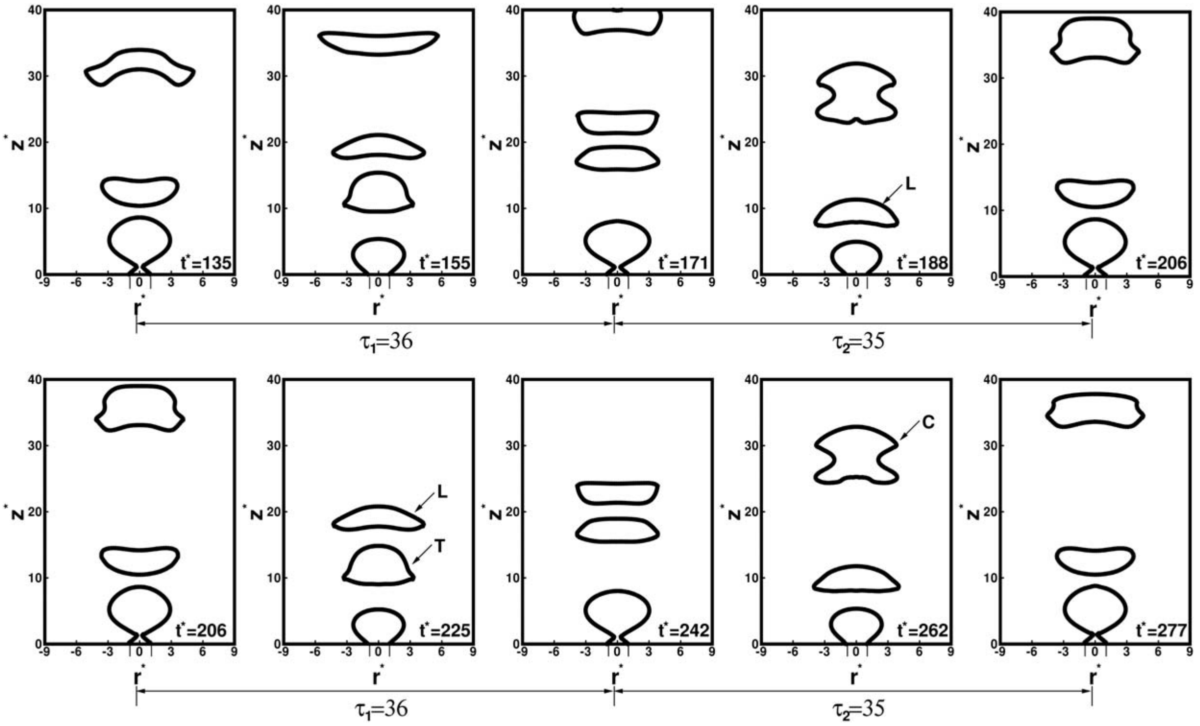

Figure 7. Period-2 with pairing and coalescence bubbling regime for *Bo* = 0.1425, *We* = 13.95, and *Re* = 2325.

L represents leading bubble, T represents trailing bubble, and C represents coalesced bubble. The other two parameters are $\eta = 6.55\times10^{-5}$ and $\lambda = 0.0112$.

dimensional growing bubble volume at the orifice for $0 \le t < 0.25s$ using the same parameters as in Figure 5. Figure 6 shows that after the first bubble detachment as in (a) and after the second bubble detachment as in (b) and (c), all consecutive detached bubbles have the same bubble volume V_b. The computed values of V_b (V_b^*) are $2.08\times10^{-8}\,m^3$ (49.30) for

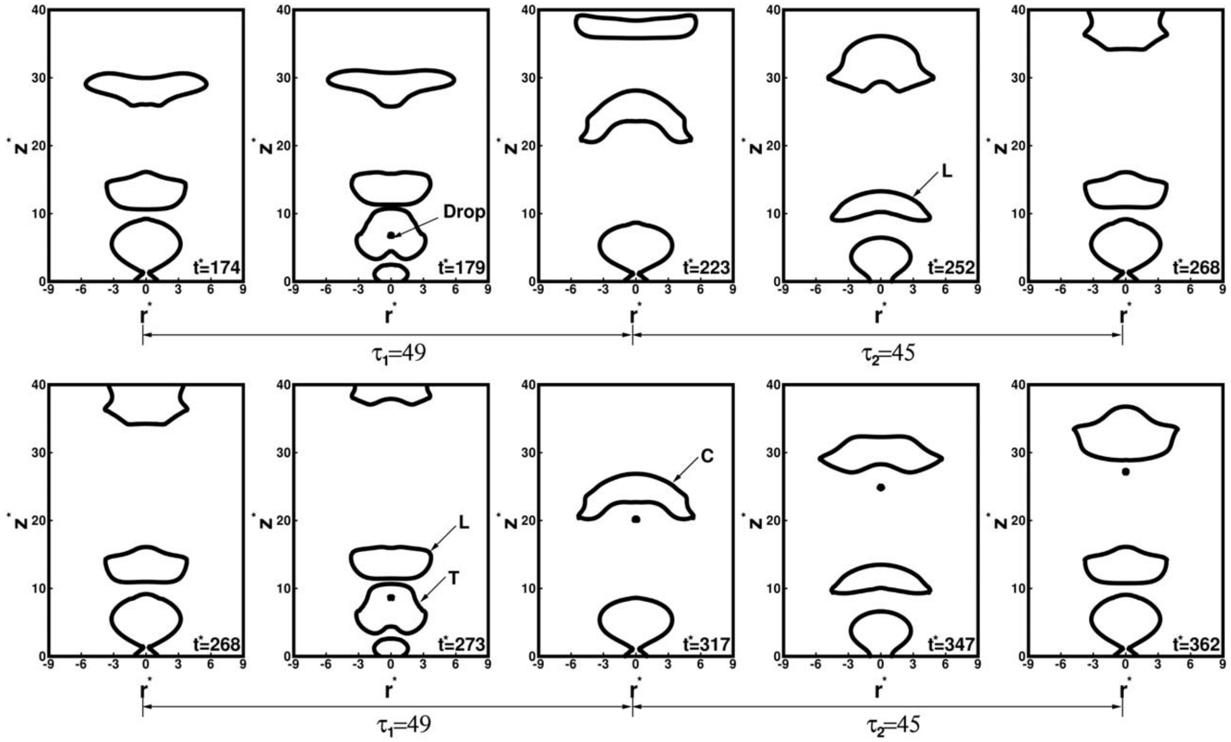

Figure 8. Period-2 with pairing and coalescence bubbling regime at higher gas flow rate for *Bo* = 0.1425, *We* = 24.81, and *Re* = 3101.25.

The other two parameters are $\eta = 6.55\times10^{-5}$ and $\lambda = 0.0112$.

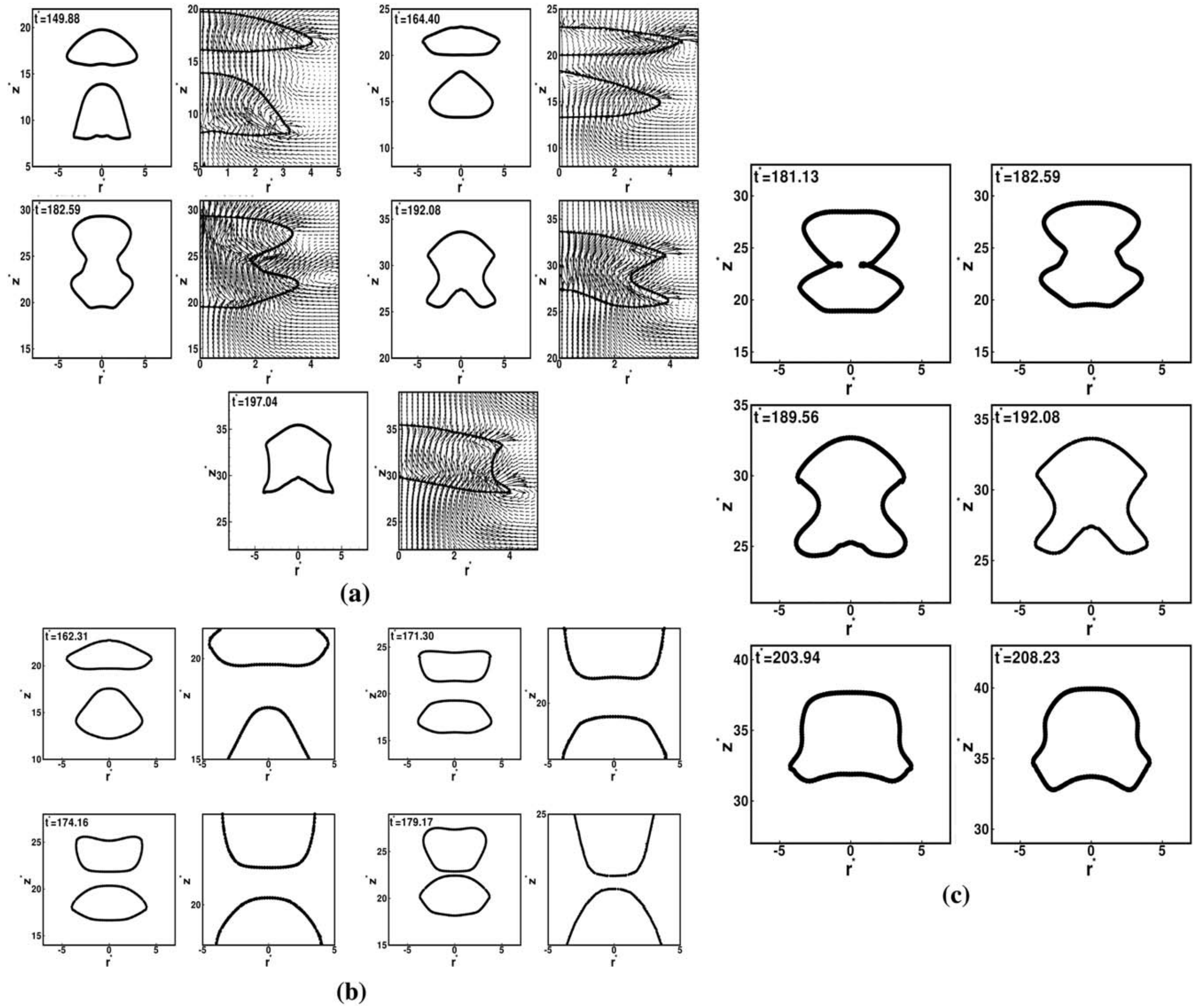

Figure 9. Time instant of (a) the shapes (left) and the corresponding velocity field (right) before and after coalescence of two coaxial (leading and trailing) bubbles, (b) film (gap) thickness and film shape and an enlarged view (right) between the leading and trailing bubbles before coalescence, and (c) after contact of two bubbles, the motions of the minimum radius of the air bridge and the shape of the coalesced bubble.

The nondimensional parameters are $Bo = 0.1425$ and $We = 13.95$ (same parameters as used in Figure 7).

$We = 0.69$, $2.805\times10^{-8}\,m^3$ (66.49) for $We = 2.76$, and $3.44\times10^{-8}\,m^3$ (81.54) for $We = 6.20$. The bubble formation process reaches a stable state after the first bubble detachment at low We (low gas flow rate) as shown in Figure 6a and after the second bubble detachment at moderate We (moderate gas flow rates) as shown in Figures 6b, c. Similar observations were reported by Ohta et al.[59] It can be expected from Figures 5 and 6 that with increasing We the bubble formation frequency increases. Figure 6 illustrates that for the period-1 bubbling regime, simulations can be carried out for the formation of 2–4 bubbles after discarding the initial transients.

Figures 7 and 8 show time sequence snapshots of bubble formation in the period-2 with pairing and coalescence bubbling regime at $Bo = 0.1425$ when $We = 13.95$ and $We = 24.81$, respectively. When We is gradually increased from 13.95 (see Figure 7), the wake behind the detached (leading) bubble begins to influence the growth of the forming bubble (trailing bubble) attached to the orifice. The liquid drag force exerted on the surface of the forming bubble is of the order $\rho_l(Q/V_b^{2/3}-v_w)^2V_b^{2/3}$ due to the wake of the leading bubble, where v_w is the average wake velocity acting on the growing bubble in the presence of the leading bubble. Owing to the reduction of the liquid drag force acting on the forming bubble, the forming bubble (trailing bubble) detaches earlier than the leading bubble and the size of the trailing bubble is smaller than that of the leading bubble (see Figure 10). As a result, the leading and trailing bubbles rise as a pair and eventually merge coaxially some distance above the orifice and a compound bubble is formed. In this regime, two distinct bubble formation periods are observed ($\tau_1 \neq \tau_2$). It is found that the bubble formation period of the trailing bubble is shorter than that of the leading bubble ($\tau_2 < \tau_1$). This regime of bubbling is known as the period-2 with pairing and coalescence bubbling regime.[20,21,23,35] With further increase in Weber number to $We = 24.81$ (see Figure 8), pairing of bubbles and coalescence move close to the orifice. The results in Figure 8 indicate that the formation periods of the trailing bubble (τ_2)

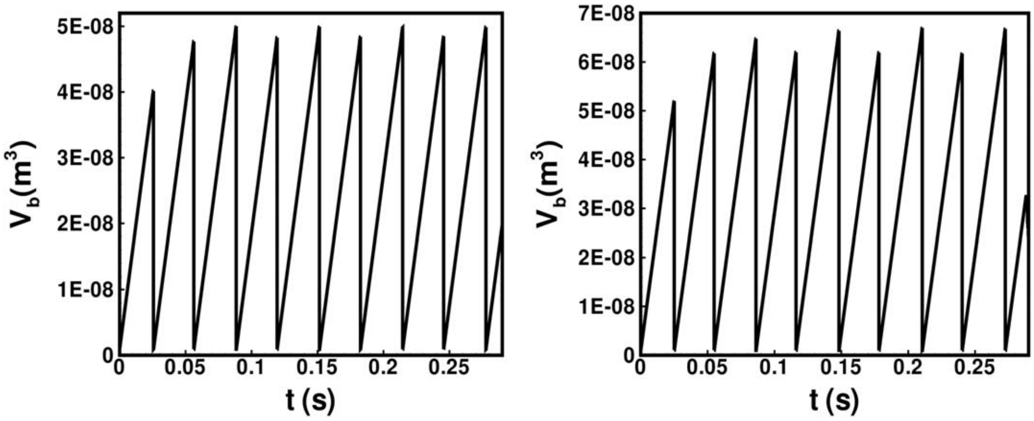

(a) We = 13.95 **(b)** We=24.81

Figure 10. Time evolution of the growing bubble volume at the orifice in the period-2 with pairing and coalescence bubbling regime for *Bo* = 0.1425 under the conditions (a) *We* = 13.95 and (b) *We* = 24.81.

are more influenced by the leading bubble (formation period of leading bubble τ_1). This is because at higher Weber number, the detached (leading) bubble becomes larger in volume and the wake behind it becomes stronger. It is interesting that the coalesced bubble does not influence the growth of the next forming bubble at the orifice and the period-2 with pairing and coalescence bubbling regime repeats. In addition, at high $We = 24.81$ a tiny liquid drop inside the detached bubble is observed, as shown in Figure 8; see Figures 4 and 6 in Ref. 35 with numerical and experimental visualizations in the high *We* region. Further, an unexpected tiny bubble is observed inside the ambient liquid; this may be due to the numerical error. In contrast, the formation of this tiny bubble may be due to the liquid drop formed inside the bubble hitting the upper part of the bubble surface after bubble coalescence. Sometimes it may not appear in the liquid, as can be seen from Figure 8. However, in this work, the formation and motion of tiny bubbles inside the ambient liquid have not been considered in detail numerically. We need more fine grids to capture this kind of tiny bubble dynamics. The same phenomena in air–aqueous glycerol solution were reported by Tufaile and Sartorelli.[27] In their experiments, tiny bubbles, known as antibubbles, were produced after the coalescence of two bubbles in the period-2 bubbling regime at high gas flow rates. An antibubble is a shell of air surrounding a drop of liquid inside the liquid. The details of anti-bubble formation are described in Ref. 27.

As noted in Figures 7 and 8, the leading and trailing bubbles rise as a pair and finally coalesce above the orifice in the liquid. This kind of interaction and coalescence between two buoyancy-driven bubbles (leading and trailing bubbles) has already been discussed in the experimental studies of Bhaga and Weber[81] and Katz and Meneveau[82] and the numerical studies of Chakraborty et al.,[76] Yuan and Prosperetti,[83] and others. Studies of two coaxial drop coalescence were reported by Manga and Stone[84] for the buoyancy-driven motion case. It is found from the results in Figure 10a (see below) that the calculated equivalent spherical bubble diameters of the leading, trailing and coalesced bubbles are 5×10^{-3}, 4.85×10^{-3}, and $6.23\times10^{-3}m$, respectively, when $We = 13.95$ and $Bo = 0.1425$ as used in Figure 7. The corresponding values of the Eotvos number are 6.33, 5.96, and 9.83, respectively. At large values of the Eotvos number greater than one, the buoyancy forces are greater than the restoring forces due to interfacial tension and a liquid jet or wake is formed behind each bubble that pushes the bottom surface of each bubble, leading to deformations, as shown in Figure 9a (see the top part, left). However, the shapes of deformed bubbles oscillate and undergo continual deformations because of the weak restoring interfacial tension forces and strong liquid inertia. Similar observations can be also made for the case in Figure 8. The results in Figures 7–9a show that the leading bubble becomes almost flattened (mostly oblate shape) whereas the trailing bubble becomes elongated (prolate shape), as observed and discussed elsewhere.[21,23,35,56,76] This prolate shape occurs due to the flow induced by the leading bubble. It can be seen that when the trailing bubble enters to the wake of the leading bubble, the drag force on the trailing bubble decreases rapidly.[76,83] As a result, the trailing bubble moves faster than the leading bubble and accelerates, which eventually causes coalescence. After coalescence, the lower surface of the coalesced bubble is accelerated to its top surface and simultaneously a liquid jet is formed behind the merged bubble, as shown in Figure 9a (see both top right and bottom parts). The coalescence occurs by the dynamics of thinning of the liquid film (see Figure 9b), which was investigated by Manga and Stone,[84] Chesters and Hofman,[85] and Oolman and Blanch.[86] It can be seen from Figure 9b that as time progresses, the film thickness decreases and the portions of the bubbles close to each other become flattened.[84–86] Once the liquid film between bubbles has substantially thinned and ruptured, the bubbles make contact. We observed from our numerical investigations that the bubbles make contact when the spacing between them is less than $110\,\mu m$. At the moment of contact of two bubbles, an air bridge with large curvature is formed. As time progresses, the bridge due to its large curvature expands in the radial direction under the influence of the Laplace pressure driving the coalescence, leading to a larger coalesced bubble with a smaller surface area [Figure 9c]. The shape (oblate/prolate) oscillations and continual deformations of the coalesced bubble can be observed (Figure 9) due to strong liquid inertia and weak interfacial stresses. The detailed analysis of the coalescence between two bubbles or drops when they are allowed to contact quasi-statically and the subsequent interfacial motion has been discussed by Stover et al.,[87] Thoroddsen et al.,[88] and Basaran.[89] The process of the coalescence of two deformable buoyancy-driven bubbles is not discussed in detail here and will be addressed further in our future work.

Table 3. The Volumes of Leading and Trailing Bubbles for $We = 13.95$ and 24.81 with $Bo = 0.1425$ in a Nitrogen–LBE System: L and T Represent Leading and Trailing Bubbles, Respectively

Volume of detached bubble	Weber number	
	$We = 13.95$	$We = 24.82$
$V^*_{b,L}$	116.023	155.918
$V^*_{b,T}$	112.69	143.95
$V^*_{b,T}-V^*_{b,L}$	3.333	11.968

Figures 10a, b show the time evolution of the dimensional growing bubble volume at the orifice for $0 \le t < 0.3$ s using the same parameters as in Figures 7 and 8, respectively. It can be seen from Figure 10 that after the second bubble detachment, bubbles of two different volumes V_b are formed successively, exhibiting the period-2 bubbling regime. The bubble formation process reaches a stable state after the second bubble detachment for the case in Figure 10a and after the fourth bubble detachment in Figure 10b. The computed values of the leading bubble volume $V^*_{b,L}$ and the trailing bubble volume $V^*_{b,T}$ when $We = 13.95$ and 24.81 are given in Table 3. It is found that the difference in the volumes of the leading and trailing bubbles ($V^*_{b,L}-V^*_{b,T}$) increases with increasing Weber number. Figure 10 shows that the number of bubbles produced remains almost the same with time $0 \le t < 0.3$ s, showing that in the high Weber number region the bubble formation frequency remains relatively constant. This regime is denoted the constant frequency bubble formation regime.[2] Figure 10 depicts that for the period-2 with pairing and coalescence bubbling regime the simulation results are consistent after the formation of 2–3 pairs and coalescence of bubbles.

Transition of bubbling regimes

Studies of the transition from period-1 to period-2 with pairing and coalescence regimes in a quiescent liquid LBE are very important for keeping bubbles small by avoiding their coalescence, which is a highly undesirable process in many industrial applications. Before discussion of the transition, we need to clarify carefully the grid refinement studies on the transition position from period-1 to period-2 with pairing and coalescence regimes. Bonometti and Magnaudet[65] reported that "the position of the transition from spherical cap to toroidal bubbles is extremely sensitive to grid resolution …." Therefore, grid sensitivity analyses on the transition positions were conducted. We studied the formation of 20 bubbles under the conditions $Bo = 0.1425$, $We = 6.20$ with a dimensionless mesh size of $\Delta r/R_o = \Delta z/R_o \approx 0.333$ (as shown in Figure 11) and $\Delta r/R_o = \Delta z/R_o = 0.2$ [as shown in Figures 5c and 6c]. For grid size $\Delta r/R_o = \Delta z/R_o \approx 0.333$, period-2 with pairing and coalescence can be observed. However, no coalescence process was seen with a grid width of $\Delta r/R_o = \Delta z/R_o = 0.2$. We also carried out the same computation using a grid size of $\Delta r/R_o = \Delta z/R_o = 0.1$ and the period-1 regime can be observed (not shown here). Therefore, we stress that grid refinement studies are needed to evaluate the accuracy of the position of the transition from period-1 to period-2 regimes. Figure 11 also indicates that the motion of the interface is not captured accurately with $\Delta r/R_o = \Delta z/R_o \approx 0.333$.

A bubbling regimes map between period-1 and period-2 with pairing and coalescence was constructed using the Bond number and Weber number in the nitrogen–liquid metal LBE system, as shown Figures 12a, b in which Bo was varied as $0.1363 \le Bo \le 2.28$. For each value of Bo, we determined the critical value of We that signals the transition from period-1 to period-2 with pairing and coalescence. The simulations were conducted using dimensionless grid sizes of 0.333, 0.2, and 0.1 to ensure the grid independence of the transition. Figure 12a indicates that the critical values of Weber number for the dimensionless grid sizes of 0.2 and 0.1 showed almost no significant changes but were very different from that for a dimensionless grid size of 0.333. It is interesting that the results follow a similar trend for three different grid sizes. The results in Figure 12a show that with increasing Bond number, the transition occurs with decreasing Weber number. The transition from period-1 to period-2 with pairing and coalescence regimes can be developed by simple scaling arguments, which have been discussed by Ambravaneswaran et al.[48] and Subramani et al.[49] for the case of transition from dripping to jetting. In the high-flow rate region and with $Oh \ll 1$, the transition occurs when the time scale $t_{f1} = \frac{\sqrt{\frac{\sigma}{\rho_l g}}}{v_{d,avg}}$ is smaller than the time scale for capillary breakup $t_c = \sqrt{\frac{\rho_l R_o^3}{\sigma}}$. The time scale t_{f1} is defined based on the capillary length scale (see Refs. 24, 25, 36, and 37) $l_c = \sqrt{\frac{\sigma}{\rho_l g}}$ (taking into account surface tension and gravity) and the average flow velocity of gas $v_{d,avg}$ at the orifice inlet. It is observed that the time scale for flow $t_f = \frac{R_o}{v_{d,avg}}$ is

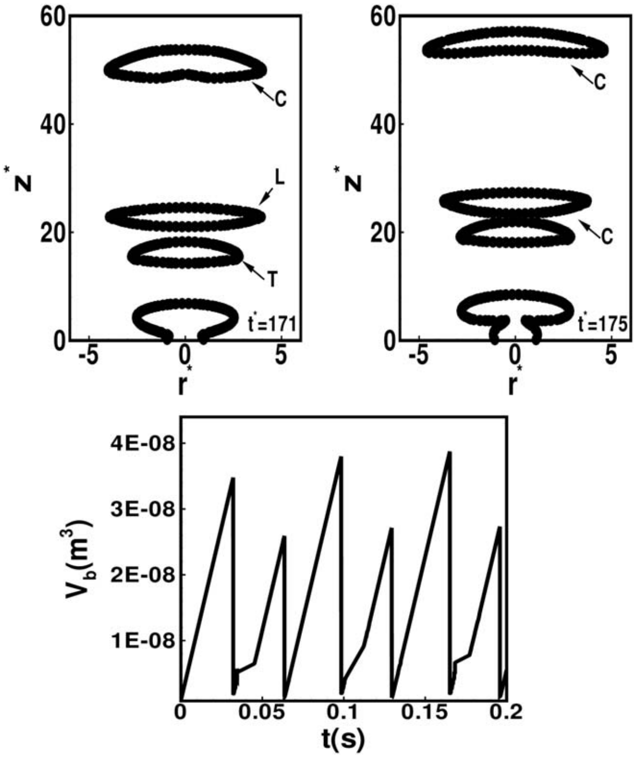

Figure 11. Evolution of bubble formation and growing bubble volume at the orifice under the conditions $Bo = 0.1425$, $We = 6.20$, $Re = 1550$, $\eta = 6.55\times10^{-5}$, and $\lambda = 0.0112$ with a dimensionless mesh size of $\Delta r/R_o = \Delta z/R_o \approx 0.333$ and pairing and coalescence is observed.

Using the same parameters, the results are shown in Figures 5(c) and 6(c) and no coalescence can be observed.

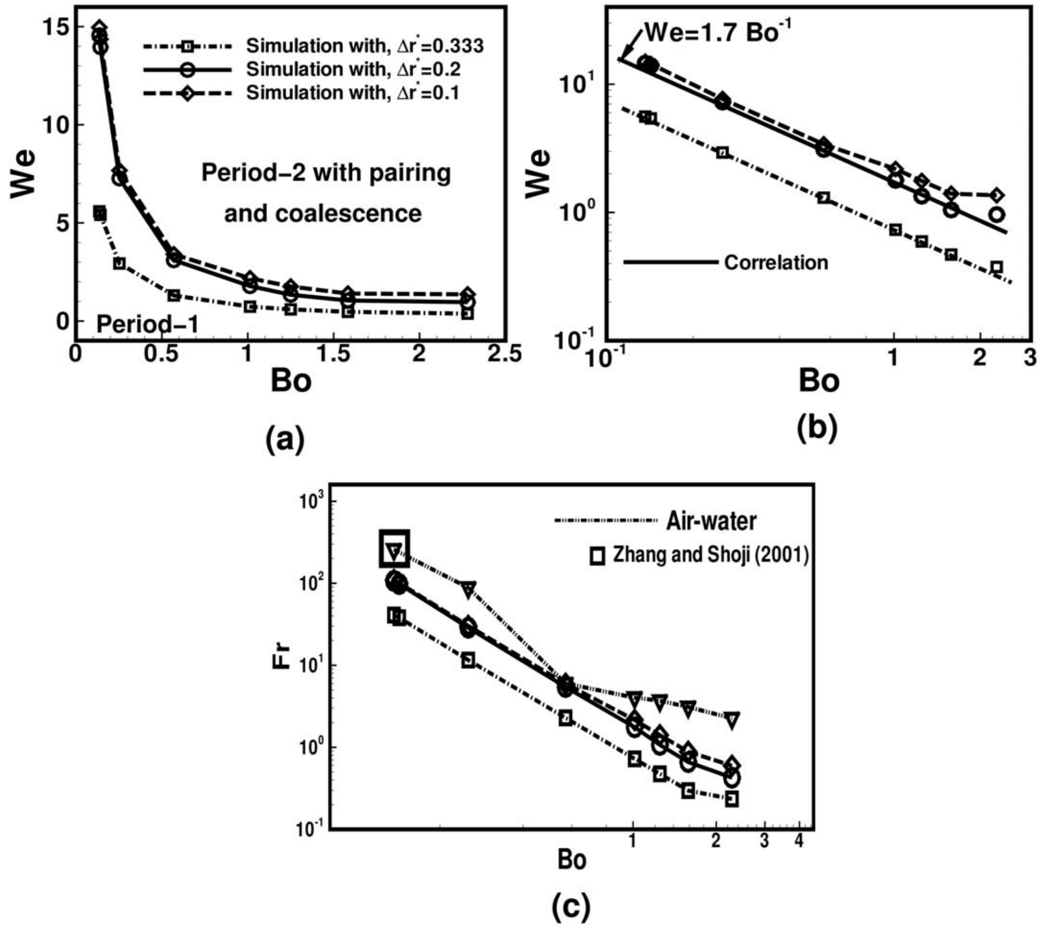

Figure 12. (a) Bubbling regimes map of the transition between period-1 and period-2 with pairing and coalescence with the help of dimensionless parameters *Bo* and *We*, (b) correlation between *We* and *Bo* for $\eta = 6.55\times10^{-5}$ and $\lambda = 0.0112$, and (c) comparison of transition from period-1 to period-2 with pairing and coalescence regimes constructed using dimensionless parameters *Fr* and *Bo* for both cases, air–water with $\eta = 0.001$ and nitrogen–LBE system with $\eta = 6.55\times10^{-5}$.

The square symbol is the transition point obtained by Zhang and Shoji[21] in an air–water system, which is at $Fr \approx 258.21$ for $Bo = 0.1363$. The predicted result from our simulation is $Fr \approx 259$ for $Bo = 0.1363$. The transition between period-1 to period-2 with pairing and coalescence is presented using dimensionless grid sizes of 0.333, 0.2, and 0.1.

also smaller than the time scale t_{f1}. By considering the condition $t_{f1} < t_c$, the transition from period-1 to period-2 with pairing and coalescence regimes occurs when $We > C\,Bo^{-1}$ for $Oh \ll 1$, where C is $O(1)$ and constant. The computed data are curve fitted to obtain correlation between We and Bo as shown in Figure 12b, where circle symbols are the computed results and the solid line is the fitted correlation. It is found that the correlation is $We = 1.7\,Bo^{-1}$, which is consistent with the scaling argument. The results in Figure 12b indicate that the critical value of We varies inversely with Bo.

Kyriakides et al.[20] and Badam et al.[23] experimentally and Buwa et al.[56] numerically reported the transition of various bubbling regimes using the Bond number ($Bo_1 = 4\rho_l g R_o^2/\sigma$) and Froude number ($Fr_1 = Q^2/2\pi^2 g R_o^5$). However, all of their results were based on an air–water system. According to our definition of Froude and Bond numbers, the relations are $Fr = 2.0Fr_1$ and $Bo = 0.25Bo_1$. Comparative results of the transitions in air–water and nitrogen–LBE systems are shown in Figure 12c in terms of Fr and Bo with different grid sizes of 0.333, 0.2, and 0.1. Figure 12c indicates that the bubble pairing and coalescence processes appear fairly early in LBE compared with those in water. Considering the air–water system, Zhang and Shoji[21] found that for $Bo = 0.1363$, the period-1 regime transits to the period-2 with pairing and coalescence regime at $Fr \approx 258.21$ [square symbols in Figure 12c] and our computed value is $Fr \approx 259$. Our predicted result agrees well with the experimental result of Zhang and Shoji.[21] For the same Bond number in the nitrogen–LBE system, we obtained the transition point at $Fr = 106.823$. Figure 12c illustrates that for the same Fr, the transition is observed in water at higher Bo compared with the case in LBE. Similarly, for same Bo, the transition is observed in LBE at lower Fr compared with the case in water. In addition, It is found from our correlation, $We = 1.7\,Bo^{-1}$, that at $Bo = 0.1$ and 1 the transition occurs when $We^{1/2} = 4.123$ and 1.304, respectively, in the nitrogen–LBE system. It is observed that the Bond number ($Bo < 0.1363$) becomes relatively insensitive to the value of the Weber number when $We > 14$ [$We^{1/2} > 3.742$; see Figure 12a]. The reason is that the period-1 regime directly transits to the period-2 with double coalescence regime. Conversely, Higuera and Medina[35] found from their numerical simulations that for the same values of Bo, the transition occurs when $We^{1/2} = 15.924$ and 6.369, respectively, in the air–water system. The substantial difference from the value of We in the transition of Higuera and Medina[35] may be due to the effect of the density of the ambient liquid and the wake effects of the detached (leading) bubble on the forming (trailing) bubble at the orifice. The liquid inertia exerted an upward force on the surface of the forming bubble of the order of $\rho_l v_w^2$ due to the averaged wake velocity, v_w, of the previous (leading) detached bubble. The stronger liquid inertia $\rho_l v_w^2$ brings about early detachment of the trailing bubble, resulting in a faster interaction and coalescence process between leading and trailing bubbles in LBE than in water.

Detached rising bubbles in a high-density liquid

From low to high gas flow rates, the calculated rising Reynolds number based on the bubble velocity and equivalent spherical detached bubble diameter in a liquid metal LBE is in the range $2000 < Re < 10{,}000$ and the Eotvos number is in the range $2 < Eo < 7$. In this range of Reynolds numbers, the motion of the detached bubbles may deviate from a vertical line and rise in a zigzag or spiral motion and the flow is nonaxisymmetric.[90–94] The path instability (zigzag or spiral) of a rising millimetric air bubble with high Reynolds numbers in water was reported by Magnaudet and coworkers[90–92] using 3-D simulations, and established that the primary cause of the onset of path instability is the wake instability in which the flow is 3-D (nonaxisymmetric) and time dependent. It was observed that the path of a rising bubble is rectilinear when the wake is axisymmetric. Magnaudet and Mougin[92] found by direct numerical simulation that when the bubble aspect ratio is $\chi < 2.21$, the flow is axisymmetric and the wake is stable whatever the Reynolds number. The bubble rises rectilinearly. Beyond $\chi = 2.21$, the 3-D flow influences the dynamics of the rising bubble and the bubble undergoes zigzag and spiral motion within a finite range of Reynolds number. They found that the flow recovers its axisymmetry again above this finite range of Reynolds number. They also reported that when $\chi = 2.5$ and $Re > 2700$, the flow returns to its axisymmetric form. Magnaudet and coworkers studied the loss of flow axisymmetric flow based on the assumption of a fixed spheroidal bubble shape. However, Cano-Lozano et al.[93] investigated the transition from straight to zigzag motion of a fixed real shape of the bubble in terms of the dimensionless parameters that govern the flow dynamics of the rising bubble. In their studies, the shape of the bubble was not considered fixed initially. The real shape of the rising bubble was obtained by means of axisymmetric computations and 3-D simulations were performed using the shape of the bubble and its terminal velocity provided by axisymmetric computations. The results obtained from their studies are more realistic. Furthermore, the stable (considered rectilinear motion) and unstable (considered zigzag or spiral motion) regions of a single bubble rising in quiescent liquids with very low values of Morton number in the range of $3.768\times10^{-4} \leq M \leq 7.710\times10^{-12}$ were discussed in detail by Cano-Lozano et al.[94] and references therein. Cano-Lozano et al.[94] using Volume of Fluid technique presented extensive numerical results for buoyancy-driven bubble motion in the stable and close to the unstable regions. The accuracy of their numerical results in terms of terminal bubble shape and terminal velocity was assessed by comparison with results of previous investigations available in the literature. The fundamental understanding of the path instability of a single bubble rising in liquids with high Reynolds number at very low Morton number is still not well established. However, a limitation of the present work is the assumption of axisymmetric fluid flows and bubble shapes.

Conclusions

We have carried out numerical simulations of the dynamics of bubble growth, generation and rising in stagnant liquids with very low Morton number, $M = O(10^{-11} - 10^{-13})$, and moderately high Reynolds number, $Re \gg 1$, using a CLSVOF method in an axisymmetric computational domain. We examined the dynamics of bubble formation for a wide range of dimensionless parameters, $4.31\times10^{-4} \leq We \leq 24.81$ and $0.13 \leq Bo \leq 2.28$, while keeping constant values of $\eta = 6.55 \times10^{-5}$ and $\lambda = 1.12\times10^{-2}$. The computations and subsequent results with respect to detached bubble volume showed good agreement with the analytical models.[22,38] It was found that the present simulations cover bubble formation from the quasi-static regime in the very low Weber number region to an inertia-dominated regime in the high Weber number region (see Figure 4). The accuracy of the computed results was assessed by comparison with scaling laws proposed in the literature[17,32] for two regimes of bubble formation: the low flow rate quasi-static regime and high flow rate dynamic regime. In this article, all the computed results are presented after careful grid refinement studies.

The present work was focused on the study of the influence of Weber number (gas flow rate) for a given Bond number (orifice diameter) on the growing bubble volume at the orifice, bubble formation frequency, detached bubble volume and the shape of the bubble. The period-1 and period-2 with pairing and coalescence bubbling regimes were discussed. At high Weber numbers, the volume (Figure 10) and departing period (Figures 7 and 8) of the leading bubbles are larger than those of the trailing bubbles, and this repeats in an alternating fashion exhibiting the period-2 bubbling regime. We also observed that during the period-1 bubbling regime, the bubble formation process reaches the steady state after the second bubble detachment whereas in the period-2 regime the steady-state bubble formation process is reached after 2–3 pairs and coalescence.

The grid refinement tests on the transition point from period-1 to period-2 with pairing and coalescence were investigated. Based on these tests, we can highlight again that the grid resolution is extremely important for finding the critical values for the transition of different bubbling regimes. In addition, the transition map shows that the system always exhibits the period-2 with pairing and coalescence bubbling regime at $We \approx 1$ when the Bond number is sufficiently high, $Bo > 2$.

It is interesting that the dynamics of bubble formation in liquid metal are identical with those of bubble formation in water when the Bond number, *Bo*, Weber number, *We*, and static contact angle, φ_s, are same in both cases. Nevertheless, we found that, even in the high Reynolds number bubble formation region, the possibility of interaction and coalescence in liquid LBE is much faster than that of water for the same value of *Bo*.

Acknowledgments

The authors wish to acknowledge financial support from a JC Bose National Fellowship of the Department of Science and Technology (DST), India. The authors are grateful to the referees for their useful suggestions.

Notation

D_o = orifice diameter, m
g = gravitational acceleration vector, m/s^2
H_ε = Heaviside function
n = normal at the interface
p = pressure, N/m^2

Q = volumetric flow rate, m^3/s
R = computational domain size, m
R_o = orifice radius, m
r = radial component of the axisymmetric coordinate, m
S = Newtonian stress tensor, N/m^2
t = time, s
u = velocity component in r direction, m/s
V = growing bubble volume at the orifice, m^3
V_b = detached bubble volume, m^3
v = velocity component in z direction, m/s
$\vec{V}$ = velocity vector (u, v)
$v_{d,avg}$ = gas mean velocity at the inlet of the orifice $(\dot{Q}_g/\pi R_{ori}^2)$, m/s
z = vertical component of the axisymmetric coordinate, m

Greek letters

α = void fraction of liquid in two-phase cell
$\tilde{\alpha}$ = smoothed void fraction field
ε = interface numerical thickness, m
η = density ratio
κ = mean curvature of the interface, m^{-1}
λ = viscosity ratio
μ = viscosity of fluid, Pa s
ρ = density of fluid, kg/m^3
σ = surface tension coefficient, N/m
τ = bubble detachment period, $(t_N^*\,(\text{at detachment of Nth bubble}) - t_{N-1}^*\,(\text{at detachment of } (N-1)th \text{ bubble})$
ϕ = level set function

Subscripts

avg = average value
cr = critical
d = disperse phase (gas)
g = gas
L = leading bubble
l = liquid
N = number of detached bubbles
o = orifice
T = trailing bubble

Superscripts

$*$ = Dimensionless quantity
$\rightarrow$ = vector
$\wedge$ = unit vector

Dimensionless numbers

Bo = Bond number
Eo = Eötvös number
M = Morton number
Re = Reynolds number
We = Weber number

Literature Cited

1. Kumar R, Kuloor NR. The formation of bubbles and drops. *Chem Eng Sci*. 1970;8:255–368.
2. Clift R, Grace JR, Weber ME. *Bubbles, Drops and Particles*. New York: Academic Press, 1978.
3. Tsuge H, Hibino SI. Bubble formation from an orifice submerged in liquids. *Chem Eng Commun*. 1983;22:63–79.
4. Kulkarni AA, Joshi JB. Bubble formation and bubble rise velocity in gas-liquid systems: a review. *Ind Eng Chem Res*. 2005;44:5873–5931.
5. Szekeley J. *Fluid Flow Phenomena in Metals*. New York: Academic Press, 1979.
6. Satyamurthy P, Dixit NS, Thiyagarajan TK, Venkatramani N, Quraishi AM, Mushtaq N. Two-fluid model studies for high density two-phase liquid metal vertical flows. *Int J Multiphase Flow*.1998; 24:721–737.
7. Li X, Tian W, Chen R, Su G, Qiu S. Numerical simulation on Taylor bubble rising in LBE using moving particle method. *Nucl Eng Design*. 2013;256:227–234.
8. Schwerdtfeger K. Velocity of rise of argon bubbles in mercury. *Chem Eng Sci*. 1968;23:937–938.
9. Mori Y, Hijikata K, Kuriyama I. Experimental study of bubble motion in mercury with and without a magnetic field. *J Heat Transf Trans ASME*. 1977;99:404–410.
10. Eckert S, Gerbeth G, Lielausis O. The behavior of gas bubbles in a turbulent liquid metal magnetohydrodynamics flow. Part I: dispersion in quasi-two-dimensional magnetohydrodynamic turbulence. *Int J Multiphase Flow*. 2000;26:45–66.
11. Zhang C, Eckert S, Gerbeth G. Experimental study of single bubble motion in a liquid metal column exposed to a DC magnetic field. *Int J Multiphase Flow*. 2005;31:824–842.
12. Andreini RJ, Foster JS, Callen RW. Characterization of gas bubbles injected into molten metals under laminar flow conditions. *Met Trans*. 1977;8B:625–631.
13. Irons GA, Guthrie RIL. Bubble formation at nozzles in pig iron. *Met Trans*. 1978;9B:101–110.
14. Bai H, Thomas BG. Bubble formation during horizontal gas injection into downward-flowing liquid. *Met Mat Trans*. 2001;32B: 1143–1159.
15. Tsuge H. Hydrodynamics of bubble formation from submerged orifices. In: Cheremisinoff NP, editor. *Encyclopedia of Fluid Mechanics*, Vol. 3. Houston, TX: Gulf Publishing. 1986:191.
16. Sadhal SS, Ayyaswami PS, Chung JN. *Transport Phenomena with Drops and Bubbles*. Berlin: Springer, 1997.
17. Davidson JF, Schuler BOG. Bubble formation at an orifice in a inviscous liquid. *Trans Inst Chem Eng*. 1960;38:335–342.
18. Ramakrishnan S, Kumar R, Kuloor NR. Bubble formation under constant flow conditions. *Chem Eng Sci*. 1969;24:731–747.
19. McCann DJ, Prince RGH. Regimes of bubbling at a submerged orifice. *Chem Eng Sci*. 1971;26:1505–1512.
20. Kyriakides NK, Kastrinakis EG, Nychas SG, Goulas A. Bubbling from nozzles submerged water: transition between bubbling regimes. *Can J Chem Eng*. 1997;75:684–691.
21. Zhang L, Shoji M. A periodic bubble formation from a submerged orifice. *Chem Eng Sci*. 2001;56:5371–5381.
22. Jamialahmadi M, Zehtaban MR, Muller-Steinhagen H, Sarrafi A, Smith JM. Study of bubble formation under constant flow conditions. *Chem Eng Res Des*. 2001;79:523–532.
23. Badam VK, Buwa V, Durst F. Experimental investigations of regimes of bubble formation on submerged orifices under constant flow condition. *Can J Chem Eng*. 2007;85:257–267.
24. Bolanos-Jimenez R, Sevilla A, Martinez-Bazan C, Gordillo JM. Axisymmetric bubble collapse in a quiescent liquid pool. II. Experimental study. *Phys Fluids*. 2008;20:112104.
25. Thoroddsen ST, Etoh TG, Takehara K. Experiments on bubble pinch-off. *Phys Fluids*. 2007;19:042101.
26. Tufaile A, Sartorelli J. Chaotic behaviour in bubble formation dynamics. *Phys A*. 2000;275:336–346.
27. Tufaile A, Sartorelli J. Bubble and spherical air shell formation dynamics. *Phys Rev E*. 2002;66:05620401.
28. Gnyloskurenko SV, Byakova AV, Raychenko OI, Nakamura T. Influence of wetting conditions on bubble formation at orifice in an inviscid liquid. Transformation of bubble shape. *Colloids Surf A*. 2003;218:73–87.
29. Byakova AV, Gnyloskurenko SV, Nakamura T, Raychenko OI. Influence of wetting conditions on bubble formation at orifice in an inviscid liquid: mechanism of bubble evolution. *Colloids Surf A*. 2003;229:19–32.
30. Wraith AE. Two stage bubble growth at a submerged plate orifice. *Chem Eng Sci*. 1971;26:1659–1671.
31. Marmur A, Rubin E. A theoretical model for bubble formation at an orifice submerged in an inviscid liquid. *Chem Eng Sci*. 1976;31:453–463.
32. Oguz HN, Prosperetti A. Dynamics of bubble growth and detachment from a needle. *J Fluid Mech*. 1993;257:111–145.
33. Wong H, Rumschitzki D, Maldarelli C. Theory and experiment on the low-Reynolds-number expansion and contraction of a bubble pinned at a submerged tube tip. *J Fluid Mech*. 1998;356:93–124.
34. Higuera FJ. Injection and coalescence of bubbles in a very viscous liquid. *J Fluid Mech*. 2005;530:369–378.
35. Higuera FJ, Medina A. Injection and coalescence of bubbles in a quiescent inviscid liquid. *Eur J Mech B*. 2006;25:164–171.
36. Longuet-Higgins MS, Kerman BR, Lunde K. The release of air bubbles from an underwater nozzle. *J Fluid Mech*. 1991;30:365–390.
37. Gerlach D, Biswas G, Durst F, Kolobaric V. Quasi-static bubble formation on submerged orifices. *Int J Heat Mass Transf*. 2005;48: 425–438.

38. Gaddis E., Vogelpohl A. Bubble formation in quiescent liquids under constant flow conditions. *Chem Eng Sci*. 1986;41:97–105.
39. Chuang SC, Goldschmidt VW. Bubble formation due to a submerged capillary tube in quiescent and coflowing streams. *Trans ASME D: J Basic Eng*. 1970;92:705–711.
40. Deshpande DA, Deo MD, Hanson FV, Oblad AG. A model for the prediction of bubble size at a single orifice in two-phase gas–liquid systems. *Chem Eng Sci*. 1992;47:1669–1676.
41. Leibson I, Holcomb E, Cacoso A, Jacmic J. Rate of flow and mechanics of bubble formation from single submerged orifices. *AIChE J*. 1956;2:300–306.
42. Tritton DJ, Egdell C. Chaotic bubbling. *Phys Fluids A*. 1993;5:503–505.
43. Zhang X, Basaran OA. An experimental study of dynamics of drop formation. *Phys Fluids*. 1995;7:1184–1203.
44. Wilkes ED, Philips SD, Basaran OA. Computational and experimental analysis of dynamics of drop formation. *Phys Fluids*. 1999;11:3577–3598.
45. Yildirim OE, Xu Q, Basaran OA. Analysis of the drop weight method. *Phys Fluids*. 2005;17:062107.
46. Ambravaneswaran B, Wilkes ED, Basaran OA. Drop formation from a capillary tube: comparison of one-dimensional and two-dimensional analyses and occurrence of satellite drops. *Phys Fluids*. 2002;14:2606–2621.
47. Ambravaneswaran B, Philips S D, Basaran OA. Theoretical analysis of a dripping faucet. *Phys Rev Lett*. 2000;85:5332–5335.
48. Ambravaneswaran B, Subramani HJ, Philips SD, Basaran OA. Dripping-jetting transitions in a dripping faucet. *Phys Rev Lett*. 2004;93:034501.
49. Subramani HJ, Yeoh HK, Suryo R, Xu Q, Ambravaneswaran B, Basaran OA. Simplicity and complexity in a dripping faucet. *Phys Fluids*. 2006;18:032106.
50. Clanet C, Lasheras JC. Transition from dripping to jetting. *J Fluid Mech*. 1999;383:307–326.
51. Eggers J, Dupont TF. Drop formation in a one-dimensional approximation of the Navier–Stokes equation. *J Fluid Mech*. 1994;262:205–221.
52. Gordillo JM, Sevilla A, Rodriguez-Rodriguez J, Martinez-Bazan C. Axisymmetric bubble pinch-off at high Reynolds numbers. *Phys Rev Lett*. 2005;95:194501.
53. Li Y, Yang G, Zhang J, Fan L. Numerical studies of bubble formation dynamics in gas–liquid–solid fluidization at high pressures. *Powder Technol*. 2001;116:246–260.
54. Chen C, Fan LS. Discrete simulations of gas–liquid bubble columns and gas–liquid–solid fluidized beds. *AIChE J*. 2004;50:288–301.
55. Gerlach D, Alleborn N, Buwa V, Durst F. Numerical simulation of periodic bubble formation at a submerged orifice with constant gas flow rate. *Chem Eng Sci*. 2007;62:2109–2125.
56. Buwa VV, Gerlach D, Durst F, Schlucker E. Numerical simulations of bubble formation on a submerged orifices: period-1 and period-2 bubbling regimes. *Chem Eng Sci*. 2007;62:7119–7132.
57. Chakraborty I, Ray B, Biswas G, Durst F, Sharma A, Ghoshdastidar PS. Computational investigation on bubble detachment from submerged orifice in quiescent liquid under normal and reduced gravity. *Phys Fluids*. 2009;21:06210301.
58. Chakraborty I, Biswas G, Ghoshdastidar PS. Bubble generation in quiescent and co-flowing liquids. *Int J Heat Mass Transf*. 2011;54: 4673–4688.
59. Ohta M, Kikuchi D, Yoshida Y, Sussman M. Robust numerical analysis of the dynamic bubble formation process in a viscous liquid. *Int J Multiphase Flow*. 2011;37:1059–1071.
60. Albadawi A, Donoghue DB, Robinson AJ, Murray DB, Delaure YMC. On the analysis of bubble growth and detachment at low capillary and Bond numbers using volume of fluid and level set methods. *Chem Eng Sci*. 2013;90:77–91.
61. Quan S, Hua J. Numerical studies of bubble necking in viscous liquid. *Phys Rev E*. 2008;77:06630301.
62. Sussman M, Puckett EG. A coupled level set and volume-of-fluid method for computing 3D and axisymmetric incompressible two-phase flows. *J Comput Phys*. 2000;162:301–337.
63. Son G, Hur N. A coupled level-set and volume-of-fluid method for the buoyancy-driven motion of fluid particles. *Numer Heat Transf B*. 2002;42:523–542.
64. Gerlach D, Tomar G, Biswas G, Durst F. Comparison of volume-of-fluid methods for computing surface tension dominant two-phase flows. *Int J Heat Mass Transf*. 2006;49:740–754.
65. Bonometti T, Magnaudet J. Transition from spherical cap to toroidal bubbles. *Phys Fluids*. 2006;18:052102.
66. Fritz W. Berechnung des maximalen Volumes von Dampfblasen. *Phys Z*. 1935;36:379.
67. Gordillo JM. Axisymmetric bubble collapse in a quiescent liquid pool. I. Theory and numerical simulations. *Phys Fluids*. 2008;20: 112103.
68. Eggers J. Nonlinear dynamics and breakup of free surface flows. *Rev Mod Phys*. 1997;69:865–929.
69. Lister JR, Stone HA. Capillary breakup of a viscous thread surrounded by another viscous liquid. *Phys Fluids*. 1998;10:2758–2764.
70. Basaran OA. Small-scale free surface flows with breakup: drop formation and emerging applications. *AIChE J*. 2002;48:1842–1848.
71. Chen AU, Notz PK, Basaran OA. Computational and experimental analysis of pinch-off and scaling. *Phys Rev Lett*. 2002;88:174501.
72. Brackbill JU, Kothe DB, Zemach C. A continuum method for modeling surface tension. *J Comput Phys*. 1992;100:335–354.
73. Osher S, Sethian LA. Fronts propagating with curvature-depending speed: algorithms based on Hamilton–Jacobi formulation. *J Comput Phys*. 1988;79:12–49.
74. Hirt CW, Nichols BD. Volume of fluid (VOF) method for the dynamics of free boundaries. *J Comput Phys*. 1981;39:201–225.
75. Harlow FH, Welch JE. Numerical calculation of time-dependent viscous incompressible flow of fluid with free surface. *Phys Fluids*. 1965;8:2182–2190.
76. Chakraborty I, Biswas G, Ghoshdastidar PS. A coupled level-set and volume-of-fluid method for the buoyant rise of gas bubbles in liquids. *Int J Heat Mass Transf*. 2013;58:240–259.
77. Gnyloskurenko SV, Nakamura T. Wettability effect on bubble formation at nozzles in liquid aluminum. *Mater Trans*. 2003;44: 2298–2302.
78. Lin JN, Banerji SK, Yasuda H. Role of interfacial tension in the formation and the detachment of air bubbles. 1. A single hole on a horizontal plane immersed in water. *Langmuir*. 1994;10:936–942.
79. Corchero G, Medina A, Higuera FJ. Effect of wetting conditions and flow rate on bubble formation at orifices submerged in water. *Colloids Surf A*. 2006;290:41–49.
80. Norman CE, Miksis JM. Dynamics of a gas bubble rising in a inclined channel at finite Reynolds number. *Phys Fluids*. 2005;17: 022102.
81. Bhaga D, Webber ME. In-line interaction of a pair of bubbles in a viscous liquid. *Chem Eng Sci*. 1980;35:2467–2474.
82. Katz J, Meneveau C. Wake-induced relative motion of bubbles rising in line. *Int J Multiphase Flow*. 1996;22:239–258.
83. Yuan H, Prosperetti A. on the in-line motion of two spherical bubbles in a viscous liquid. *J Fluid Mech*. 1994;278:325–349.
84. Manga M, Stone HA. Buoyancy-driven interactions between two deformable viscous drops. *J Fluid Mech*. 1993;256:647–683.
85. Chesters AK, Hofman G. Bubble coalescence in pure liquids. *Appl Sci Res*. 1982;38:353–361.
86. Oolman TO, Blanch HW. Bubble coalescence in stagnant liquids. *Chem Eng Commun*. 1986;43:237–261.
87. Stover RL, Tobias CW, Denn MM. Bubble coalescence dynamics. *AIChE J*. 1997;43:2385–2392.
88. Thoroddsen ST, Etoh TG, Takehara K, Ootsuka N. On the coalescence speed of bubbles. *Phys Fluids*. 2005;17:071703.
89. Basaran OA. Nonlinear oscillations of viscous drops. *J Fluid Mech*. 1992;241:169–198.
90. Magnaudet J, Eames I. The motion of high-Reynolds-number bubbles in homogeneous flows. *Annu Rev Fluid Mech*. 2000;32:659–708.
91. Mougin G, Magnaudet J. Path instability of a rising bubble. *Phys Rev Lett*. 2002;88:14502.
92. Magnaudet J, Mougin G. Wake instability of a fixed spheroidal bubble. *J Fluid Mech*. 2007;572:311–337.
93. Cano-Lozano JC, Bohorquez P, Martinez-Bazan C. Wake instability of a fixed axisymmetric bubble of realistic shape. *Int J Multiphase Flow*. 2013;51:11–21.
94. Cano-Lozano JC, Bolanos-Jimenez R, Gutierrez-Montes C, Martinez-Bazan C. The use of volume of fluid technique to analyze multiphase flows: specific case of bubble rising in still liquids. *Appl Math Model*. 2015;39:3290–3305.

Manuscript received Sep. 15, 2014, and revision received Apr. 29, 2015.